Depletion Induced Bundling of Rod-Like Colloids and Simulations of Triple Helix Bundles

by

Jonathan Adams

A thesis submitted to the School of
Graduate and Postdoctoral Studies in
partial fulfillment of the requirements for
the degree of

MSc in Modelling and Computational Science
The Faculty of Science

University of Ontario Institute of Technology (Ontario Tech University)

Oshawa, Ontario, Canada

June 2023

THESIS EXAMINATION INFORMATION

Submitted by Jonathan Adams

MSc in Modelling and Computational Science

Thesis title: Depletion Induced Bundling of Rod-Like Colloids and Simulations of Triple Helix Bundles

An oral defense of this thesis took place on May 25th 2023 in front of the following examining committee:

Examining Committee

Chair of Examining Committee	Dr. Greg Lewis
Research Supervisor	Dr. Hendrick de Haan
Examining Committee Member	Dr. Lennaert van Veen
Thesis examiner	Dr. Theresa Stotesbury, Ontario Tech University

The above committee determined that the thesis is acceptable in form and content and that a satisfactory knowledge of the field covered by the thesis was demonstrated by the candidate during an oral examination. A signed copy of the Certificate of Approval is available from the School of Graduate and Postdoctoral Studies.

Abstract

We ran molecular dynamics simulations of rod-like colloids acting under depletion forces. In these simulations, we found bundling of the rods above a given strength of the depletion force. We then analyzed the bundle formation process and how the shape and flexibility of the rods could effect bundle formation. We then looked at preferential bundling of long or stiff rods, and the hysteresis of bundle formation.

We also collaborated with Vincent Tabard-Cossa's lab at UOttawa to analyze the unexpected experimental behaviour of triple helix bundles folding through a nanopore. We ran coarse grained molecular dynamics simulations of 3HB to gain insight into the translocation process, and into the potential causes of the unexpected folding behaviour.

Keywords: Depletion Force, Molecular Dynamics, Nanopore

Declaration of Authorship

- I hereby declare that this thesis consists of original work of which I have authored. This is a true copy of the thesis, including any required final revisions, as accepted by my examiners.
- I authorize the University of Ontario Institute of Technology (Ontario Tech University) to lend this thesis to other institutions or individuals for the purpose of scholarly research. I further authorize Ontario Institute of Technology (Ontario Tech University) to reproduce this thesis by photocopying or by other means, in total or in part, at the request of other institutions or individuals for the purpose of scholarly research. I understand that my thesis will be made electronically available to the public.

Signed:

_____

Date:

_____

Statement of Contributions

The work described in Chapter 3 was begun during the author's undergraduate thesis. While many of the qualitative results are similar, all of the simulations have been totally redone, and all of the analysis has been significantly expanded.

The work described in Chapter 4 was collaboration with Vincent Tabard-Cossa's lab at UOttawa. This group is currently publishing a paper on the experimental behaviour of triple helix bundles folding through a nanopore [12]. While the simulations described in chapter 4 were not used in the paper, they helped understand what was happening in experiments.

Acknowledgements

First I would like to acknowledge my supervisor Hendrick de Haan, who has been extremely patient with me over the course of my Masters', and has given me every opportunity to succeed. I would also like to acknowledge the members of the CNabLab who were present over the course of my Masters'. The discussions I've been a part of over the course of my studies greatly expanded my point of view and being around such a talented group has enriched my life greatly. In particular, I would like to thank Saadat Shah for proof reading much of this thesis.

I would also like to thank Vincent Tabard-Cossa's lab at UOttawa, for the opportunity to collaborate with them. Vincent Tabard-Cossa, Kyle Briggs, Martin Charon, and Liqun He are all extremely skilled and intelligent, and the ability to collaborate with them was a gift.

I would like to thank my parents, Doug and Elaine, mainly for subsidizing my life with free food, but also for being there when I needed them. Most of all I would like to thank my brother Daniel. Without my brother's ironclad and enduring support this thesis would have been impossible.

Finally, I would like to thank my friends Ryan Ash and Isaac Maclean. Ryan's extensive knowledge of biology was frequently invaluable. Isaac's constant presence in my life kept me sane, and I am forever indebted.

Contents

List of Figures

List of Tables

List of Abbreviations

PEG	**P**oly**E**thylene **G**lycol
MD	**M**olecular **D**ynamics
LD	**L**angevin **D**ynamics
MFPT	**M**ean **F**irst **P**assage **T**ime
3HB	Triple **H**elix **B**undle
dsDNA	**d**ouble **s**tranded **D**eoxyribo**N**ucleic **A**cid
ssDNA	**s**ingle **s**tranded **D**eoxyribo**N**ucleic **A**cid

Physical Constants

Boltzmann Constant $k_b = 1.38 * 10^{-23}\ m^2\ kg\ s^{-2}\ K^{-1}$

List of Symbols

l_p	Persistence Length	[length]
V_0	Simulation Voltage	[mass][length]^2[time]$^{-2}$[charge]$^{-1}$
σ	Simulation Distance Unit	[length]
τ	Simulation Time Unit	[time]
ϕ	Depletant Fraction	
ΔU	Energy Barrier	[mass][length]^2[time]$^{-2}$

Chapter 1

Introduction

The two main topics of this thesis are Depletion Induced Bundling of Rod-Like Colloids and Simulations of Triple Helix Bundles. Both of these systems involve the dynamics of nanoscopic to microscopic objects in a fluid. We investigate these systems with computer simulations. Simulation studies can provide insight into systems which are difficult to study experimentally.

1.1 Coarse Grained Molecular Dynamics

We implement Coarse Grained Molecular Dynamics. Molecular Dynamics (MD) is a simulation method which uses Newton's equations of motion to integrate a system forward in time. Suppose one has the positions of all the particles in a system, and the forces each particle exerts on the others, as well as external forces acting on the particles. In this case, it is possible to numerically integrate the system to find each particle's new positions and velocities. We can repeat this process an arbitrary number of times to continually integrate our system forward in time. Newton's laws of motion are accurate even at the molecular level, thus as long as we specify the correct forces between particles, the system will evolve physically reasonable way.

Atomistic MD simulations model every atom as a particle. However, simulations which are accurate to the molecular level of colloids or dsDNA tend to have millions of particles. This many particles would be far too many for our simulations to be computationally feasible. Instead, we aggregate groups of particles in the system into single spherical particles, with physical properties

representing the average of the aggregate. In this way, we give up the fine details of a system for computational efficiency. This process is known as "coarse graining", and we want to coarse grain the system such that the most important characteristics of the system are preserved. In this work, we are particularly concerned with the effects of length and persistence length of objects, and their effect on the dynamics of a system.

1.1.1 Langevin Dynamics

Our simulations model systems situated within a solvent. Explicitly modelling the solvent is computationally unfeasible due to the number of additional solvent particles that need to be simulated. In order to model the solvent, we use Langevin Dynamics (LD) to model it implicitly. Langevin Dynamics models the solvent as two additional forces applied to all particles in the simulation. The first force is a linear drag term, to model the viscosity of the fluid. The second is a random fluctuation term that models the solvent particles interactions with the structures of interest. This approach assumes that the solvent acts independently on every particle in the system. A fundamental disadvantage of LD is that it does not model any hydrodynamical phenomena, such as fluid interaction with solid boundaries.

1.2 Depletion Induced Bundling of Rod-Like Colloids

The Depletion Force is an attractive entropic force between colloids in a bath of significantly smaller particles. These smaller particles are known as depletants. There are two main ways to conceptualize the Depletion Force (Figure 1.1). The first is the entropic picture. The center-to-center distance between a spherical depletant and a spherical colloid is at minimum $R_c + R_d$, where R_c is the radius of a colloid and R_d is the radius of the depletant. We consider a volume within R_d of the colloid to be the excluded volume of the colloid, as the center of a depletant cannot be within this region. When two colloids are in contact with

each other, their excluded volumes overlap, and the free volume in the system the depletants are able to occupy increases by the amount equal to the volume of the overlap. Thus, it is entropically favorable for the depletants when the colloids are packed together such that their excluded volumes heavily overlap. However, packing the colloids together is not entropically favorable for the colloids. When the number of depletants is low, the entropy gain from overlapping the excluded volumes of the colloids is not enough to offset the entropy loss by restricting the colloids to be packed together. As the number of depletants in the system increases, the entropy gain from overlapping the excluded volumes increases, and with enough depletants, the entropy gain associated with the additional volume available to the depletants becomes larger than the entropy loss from packing the colloids together, and the colloids become packed together.

The other picture is the kinetic picture. When the colloids are far apart, they are bombarded by the depletant particles from all sides. Normally, this results in Brownian motion. However, when the excluded volumes overlap, the that depletants cannot occupy the space between the colloids. As a result, the colloids are bombarded from every direction except the direction of the nearby colloid. This induces a net force on the colloids toward one another. With enough depletants, this induced force can overcome the thermal fluctuations that would otherwise separate the colloids, causing them to "stick" together.

1.2.1 Depletion Force Acting Between Rods

Our lab has previously researched aggregation of blood cells into rouleaux structures and investigating depletion forces as a potential cause [18]. Using similar simulation methods, we set out to model the aggregation of rods. Many biological systems, particularly inside cells, are crowded environments, with large structures surrounded by high concentrations of macromolecules which can cause depletion effects. In addition, many rod-like objects exist in these environments. Actin filaments in cells can be forced together in cells via depletion forces (Seen in Figure 1.2) [22] [16], rod-like *fd* viruses can be used to form membranes [25], and crowded environments can cause fibrous collagen to form larger structures [20]. It would be remiss of us to forget that Tobacco Mosaic Virus is another

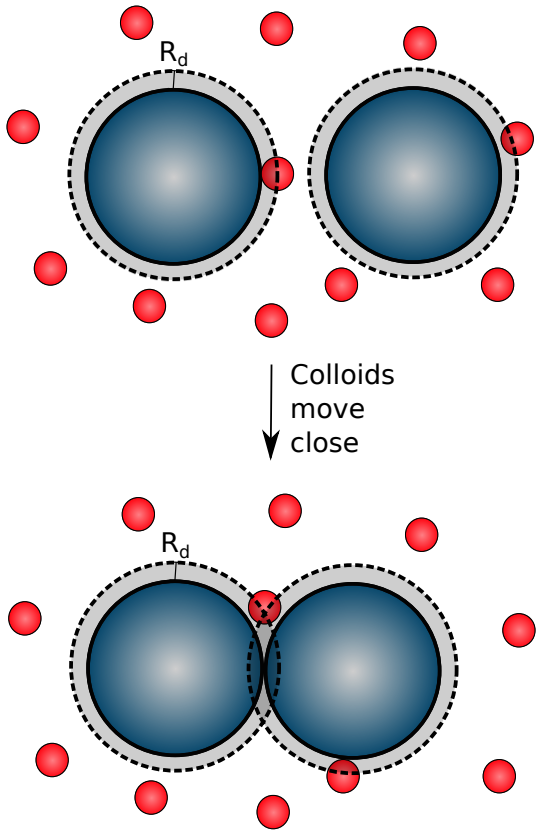

FIGURE 1.1: Schematic of Depletion Force and Excluded Volume. The blue particles are the colloids, the red particles are the depletants, and the grey area around the colloids is the excluded volume. Note that when the colloids are close, the excluded volume is overlapped. In addition, the depletants cannot fit between the colloids when the colloids are close together.

commonly studied rod-like colloid [6] [9]. In these systems, example depletants are particles like polyethylene glycol and dextran.

The density of the rod mixture is important when discussing the phase behaviour. Many studies work with systems of rods at large densities [7]. In our simulations, coming from working with relatively low density blood cells, and playing to the strengths of MD simulations, we performed simulations of relatively low densities of rods. S.S. Cohen (1942) [6] notes formation of crystals and precipitation of Tobacco Mosaic Virus and other biological rods at low densities of the virus, and we believe our simulations are most analogous to these

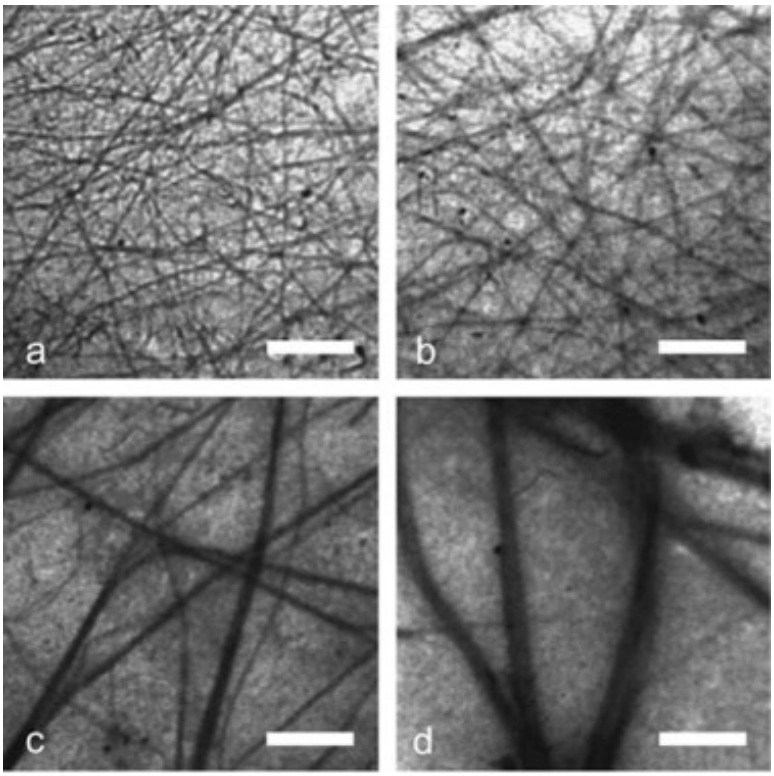

FIGURE 1.2: Electron Microscopy Pictures of actin filaments from R. Tharmann (2006) [22]. The scale bar is 0.5 μm. In these experiments, polyethylene glycol (PEG) with an average molecular weight of 6k daltons is used as a depletant. In *a*, there is no PEG. In *b*, *c*, and *d*, PEG is added to the system with a concentration of 1.5 %, 4%, and 8 % weight/weight respectively. The actin filaments form increasingly large bundles as the PEG concentration increases. Reprinted from Biophysical Journal, Vol 90, R. Tharmann, M.M.A.E. Claessens, A.R. Bausch, Micro- and Macrorheological Properties of Actin Networks Effectively Cross-Linked by Depletion Forces, pg 2622-2627, Copyright (2006), with permission from Elsevier.

systems. In particular, our systems of many rods saw a nucleation process, where small bundles of rods were unstable while large bundles of rods were stable. A. Cuetos, M. Dijkstra (2007) [7], is a simulation study of structures made up of rods which also notes the nucleation process.

Our goals for this work were to use MD simulations of rods to investigate the

structures that might be formed at sufficiently high depletant fractions, similar to previous work done in the lab on blood cells [18]. From there, we wanted analyze how the rods shape and stiffness might influence the structures formed, or what depletant fractions the structures would be formed at.

This work represent an significant expansion on the author's undergraduate thesis. While many of the qualitative results are similar, the simulations were all completely redone, and the analysis presented here is much deeper than that of earlier work, particularly with respect to the energy associated with bundling.

1.3 Triple Helix Bundles

Our simulations related to nanopores and Triple Helix Bundles (3HB) were carried out to assist Vincent Tacard-Cossa's lab at UOttawa. Our goals were to model the 3HB in simulation, gain insight into the dynamics of 3HB close to a nanopore, and shed light on the unexpected folding behaviour of 3HB.

1.3.1 Structure of Triple Helix Bundles

3HBs are a nanoscopic structure created using DNA origami [19]. The structure can be described roughly as three strands of dsDNA woven together. A long scaffold strand of ssDNA is folded into shape by many smaller staple strands of ssDNA, which can only bind to the scaffold strands at specific points. This process is shown in Figure 1.3.

A visualization of the 3HB and scaffold staple structure can be seen in Figure 1.4. The 3HBs used by UOttawa were 2249 base pairs long, corresponding to a length of about 820 nm. Given that the structure is effectively three dsDNA strands stapled together, we expected it to be significantly stiffer than dsDNA.

1.3.2 Nanopores

Nanopores are nanoscopic holes in a membrane which is also of nanoscopic thickness. Typical values for the size of a nanopore used by our collaborators at

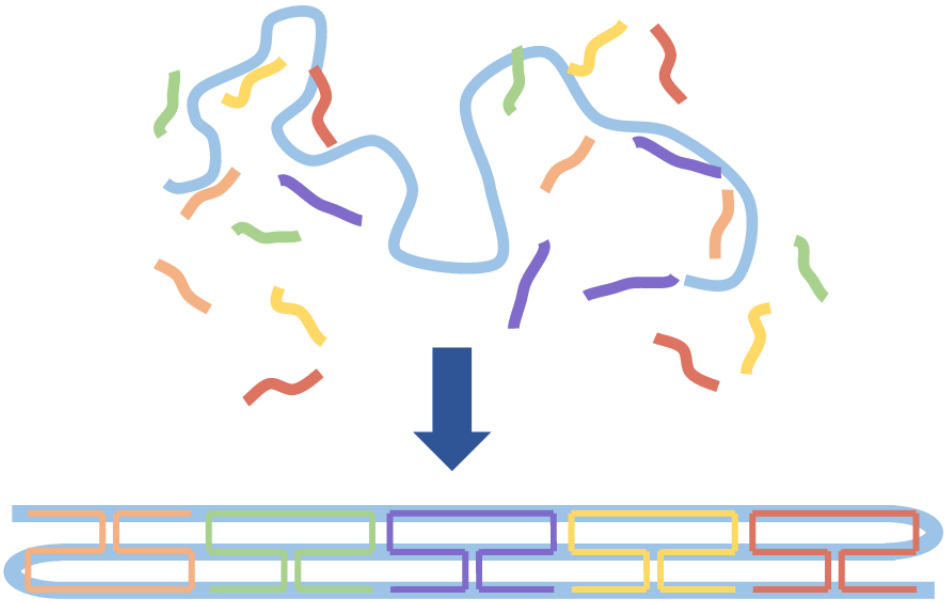

FIGURE 1.3: Figure from He et al. (2023) [12], of the formation of 3HB from the colored staple strands and the light blue scaffold strand. The staples can only bind to the scaffold at particular points. Used with permission.

UOttawa is a diameter of between 9 nm and 15 nm, and a pore thickness of between 9 nm and 15 nm.

A voltage is applied across the pore, which drives charged objects through the pore. Polymers are placed on the side of the pore we term the cis side, and the voltage is applied such that objects are driven through the pore to the other side, which we term the trans side. A polymer which crosses the pore from the cis side to the trans side is consider to have "translocated" through the pore. We will use this term frequently throughout this work. Figure 1.5 shows a schematic of the pore, and a polymer translocation.

A current is run across the pore, and when a polymer is inside the pore, that current is partially blocked. The magnitude of the blocked current is dependent on the structure and configuration of the polymer. This allows one to know when a polymer translocates, and by examining the magnitude of the blocked current, they can determine what kind of polymer translocated. They can even gain insight into how the polymer entered the pore. This blockage current can also

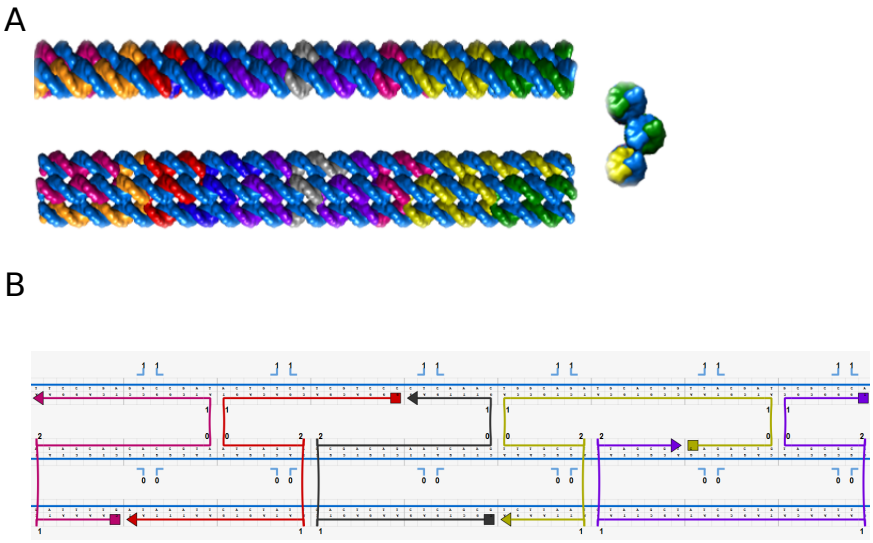

FIGURE 1.4: A) Visualization of Triple Helix Bundle from multiple angles from He, L (2022) [11]. B) Picture of the scaffold and staple of the Triple Helix Bundle, from He, L (2022). The light blue strands are the scaffold strand, and the other colors are staple strands. Both are used with permission

detect polymers stuck at the pore, as a small length of the polymer can bend into the pore and disrupt the current. Analysis of the current blockage can be used in the detection of biomarkers [3] [4].

The blocked current can also help determine what configuration the polymer translocated in (Figure 1.6). If a polymer approaches the nanopore by an end and threads through, it will have a given current blockage. If a polymer approaches the nanopore by the middle and folds through the pore, the current blockage will be different from the unfolded event. The UOttawa group even saw more complicated folding events, but our work was concerned with folded and unfolded events.

1.3.3 Folding Question

The UOttawa group ran experiments of 3HB and dsDNA strands of an equivalent length translocating through the pore. When examining the number of folded

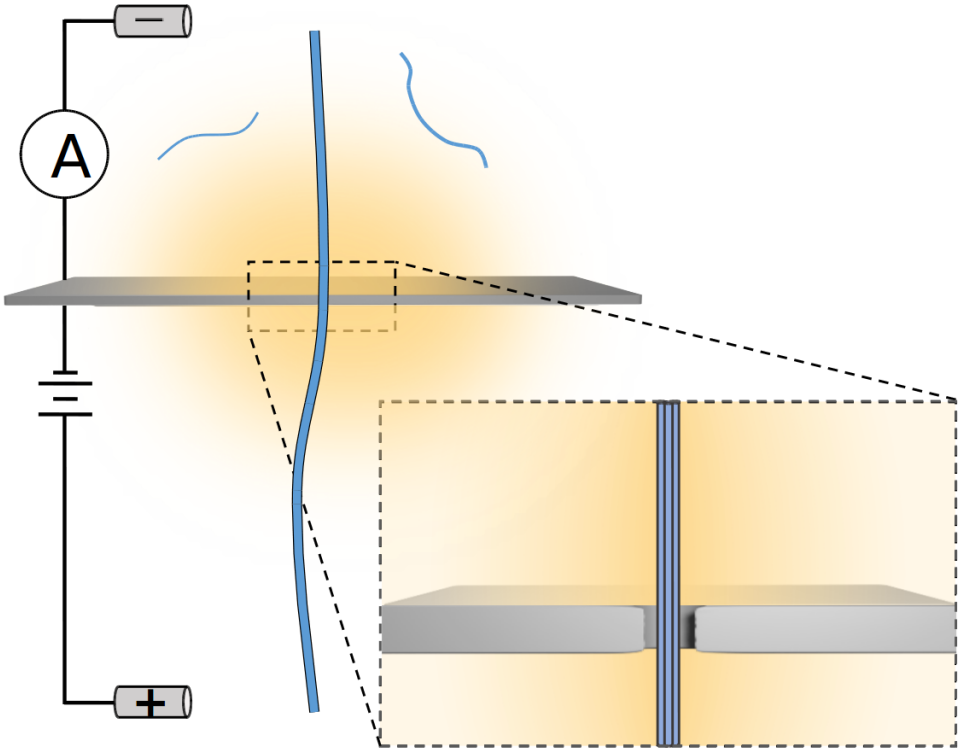

FIGURE 1.5: Schematic of polymer threading through the pore, from He et al. (2023). The yellow hue represents the electric field strength. The 3HB is driven from the top (cis) side of the pore to the bottom (trans) side of the pore by the electric field. When the 3HB is inside the pore, it partially blocks current across the pore, which can then be detected. Used with permission.

events for 3HB, it was found that the 3HB folded significantly more than dsDNA of equivalent lengths (Figure 1.7).

Since we expected 3HB to be much stiffer than dsDNA, we expected it to fold less, mainly because it would take significantly more energy to fold 3HB through the pore, if it could fold through at all. We also expected the increased stiffness to affect how 3HB approached the pore, but it was unclear whether it would result in more or less folding. The increased folding of 3HB occurred even at the lowest voltages the UOttawa group tested.

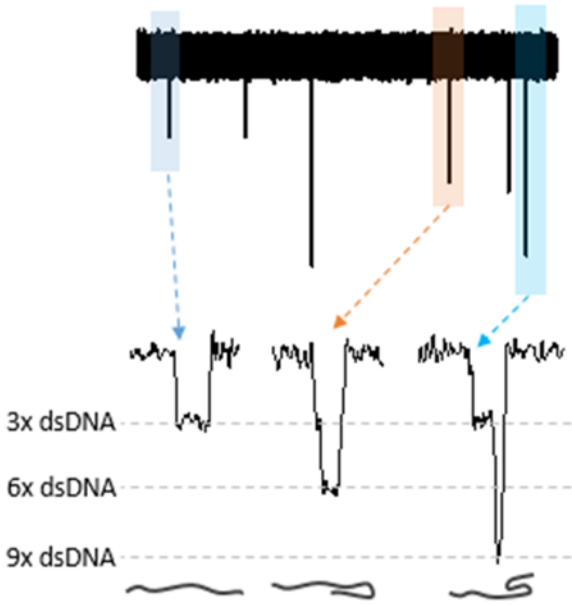

FIGURE 1.6: Blockage levels of the Triple Helix Bundles, from He, L (2022). Translocation events can be categorized by the maximum current blockage. Here, an unfolded event has 3 times the current blockage of unfolded dsDNA, while a folded event has 6 times the current blockage. More complicated folded states could also be distinguished using this technique. Used with permission.

1.3.4 Defect Hypothesis

We posited that defects in the structure of the 3HB could be responsible for the increased folding behaviour. It is suspected that staple strands could be not completely stapled on to the scaffold, that some strands may not have bound to the scaffold at all, or that staple strands might be disrupted near the pore. Even if the structure was perfectly assembled, it was possible that the staple-scaffold structure was not uniformly stiff across the entire length.

As the research had progressed, the UOttawa group found results which were indicative that the polymer required defects to fold through the pore. Figure 1.8 shows experimental results from the UOttawa group that the time that the 3HB structure would remain stuck at the pore before translocating would increase as the voltage increased. If 3HB could fold through the pore without a defect, this is

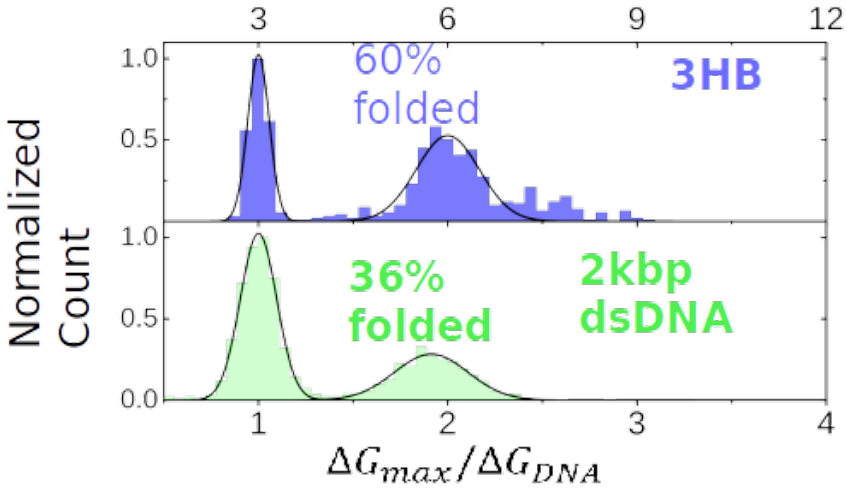

FIGURE 1.7: Histograms of translocations events from UOttawa, He et al. (2023). The results were from a nanopore 13.3 nm in diameter, with 200 mV across it. The x axis is the current blockage of a translocation, normalized by the current blockage of dsDNA. For both 3HB and dsDNA, the distributions are bimodal, with the left mode representing the single file translocations, and right mode representing the folded translocations. Here 3HB folds significantly more than dsDNA of a similar length. This result was seen across various pore sizes and voltages. Used with permission.

not what we would expect; an increase in the voltage should decrease the energy barrier associated with folding since the electric force pulling the 3HB through the pore should be greater. Thus, the time polymers spend stuck at the pore should go decrease. However, consider an alternate picture, seen in Figure 1.9. If we assume that 3HB requires a defect to fold through the pore, then the time that a polymer stays stuck at the pore is dependent on the time taken for a weak point of 3HB to reach the nanopore and fold through. Increasing the voltage in this case can reduce lateral diffusion of the 3HB, by increasing pore friction or by other means. This would explain the counterintuitive results seen in Figure 1.8.

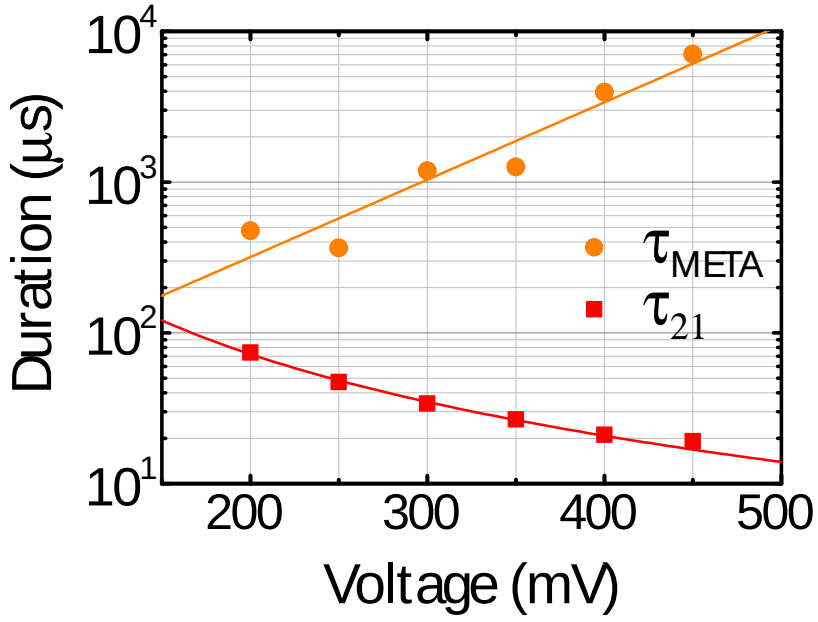

FIGURE 1.8: Plot of the duration of metastable states (τ_{META}) and translocation time (τ_{21}) of experiments of 3HB translocating through nanopores. From He et al. (2023). In this case the metastable states are where 3HB is stuck at the pore, and the translocation time is how long it takes to move through the pore after it breaks out of the metastable state. We expect the duration of the metastable states to go down with voltage if the polymer is not defective. Used with permission

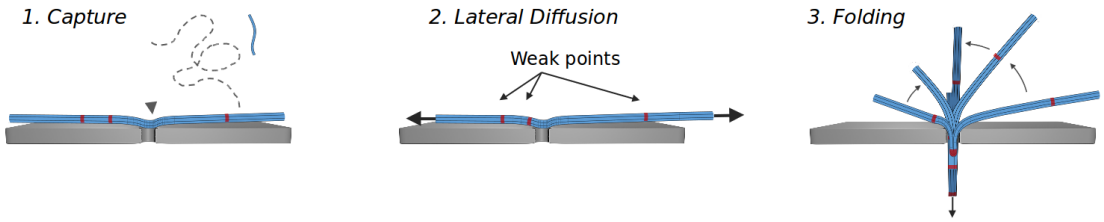

FIGURE 1.9: Picture of the proposed folding process from He et al. (2023). First, the 3HB approaches the nanopore by its center. It is unable to fold through without a defect, and it diffuses laterally until a defect is above the nanopore, at which point it is able to fold through through. Used with permission.

Chapter 2

Methodology

2.1 Introduction

We use Coarse Grained Molecular Dynamics to investigate bundling of rod-like colloids, and triple helix bundles translocating through a nanopore. We will start by going through simulations specifics common to both projects, then focus on particulars for each project. All the simulations detailed in this thesis were done using HOOMD-Blue toolkit [1].

2.2 Equations Of Motion

As stated before, we used Coarse Grained Molecular dynamics to conduct our simulations. Fundamentally, Molecular Dynamics is simply numerically integrating Newton's Second Law over time for every particle in the system at each time step. We will start with Newton's Second Law

$$\sum \vec{F} = m\vec{a} \tag{2.1}$$

If we compute all the forces acting on a particle at time t, we can find its acceleration at time t. With the acceleration known, HOOMD-Blue uses the Velocity-Verlet algorithm to find the particle's position and velocity at $t + \Delta t$, where Δt is the timestep of our simulation. This process integrates the particle forward Δt in time. If we do this for every particle, we have moved the system forward Δt in time, and we can repeat this process to move it forward an

arbitrary amount of time. In our simulations of 3HB, $\Delta t = 0.01$, and in our rod-like colloid simulations $\Delta t = 0.005$.

This alone would be sufficient for particles in a vacuum, but we are investigating objects which exist in fluid. In order to avoid explicitly simulating the fluid, we use Langevin Dynamics, which uses the following forces.

$$\sum \vec{F} = \gamma\vec{v} + \vec{F}_R + \vec{F}_{Other} \tag{2.2}$$

The first term $\gamma\vec{v}$ accounts for the viscosity of the fluid. It is a linear drag term, with γ being the drag coefficient in our simulation, and $\vec{v}$ being the velocity of the particle. At the scales which we are investigating in our simulations, drag forces are linear. Note that we set $\gamma = 1$ for all of our simulations.

The second term $\vec{F_R}$ accounts for the jostling of the particle by smaller fluid particles. To model this, $\vec{F}_R$ is a random force applied at each time step. The magnitude and direction of $\vec{F}_R$ is drawn from a uniform distribution, such that the net force averages out to 0,

$$\langle \vec{F}_R \rangle = 0 \tag{2.3}$$

Which is to say that no direction is preferred. In addition, the magnitude is chosen such that the variance is as follows

$$\langle |\vec{F}_R|^2 \rangle = 6k_bT\gamma/\Delta t \tag{2.4}$$

where k_b is the Boltzmann constant, T is the temperature of our system, and Δt is the size of our timestep.

The final term, $\vec{F}_{Other}$, are simply the other forces present in our system. The other forces will have a potential energy associated with them such that

$$\vec{F} = -\nabla V(r) \tag{2.5}$$

Where $\vec{F}$ is a force and $V(r)$ is the potential energy associated with that force.

Newton's laws are easiest to implement on spherical objects, as there is no need to take into account torque on a spherical object. We used spherical beads

as the base building blocks of our simulations. Larger structures were created out of many beads by applying potentials between them.

2.2.1 The Lennard-Jones and WCA Potentials

Realistically, particles cannot physically overlap, and we needed a force to model the particles inability to overlap. When the beads are overlapped, it should be large, and it should be zero when they are not overlapped. Additionally, we needed the force to be continuous. We started with the Lennard-Jones (LJ) potential [13], given by

$$V_{LJ}(r) = 4\epsilon \left[\left(\frac{\sigma}{r}\right)^{12} - \left(\frac{\sigma}{r}\right)^{6} \right] \tag{2.6}$$

Where σ is the radius of the bead, ϵ is the strength of the force, and r is the distance between the two beads.

The LJ potential is an extensively used potential in molecular dynamics, used to model intramolecular forces, including repulsion. It is well understood, has a strong repulsive force when the particles are overlapped, and quickly goes to zero when the particles are not overlapped. The only problem with the LJ potential is that it is an attractive potential when the particles are further than $2^{\frac{1}{6}}\sigma$ apart from one another. We can fix this by simply truncating the potential after $r = 2^{\frac{1}{6}}\sigma$, and shifting the potential up, such that the energy is zero at $r = 2^{\frac{1}{6}}\sigma = R_{cut}$. This shifted and truncated version of the LJ potential is called the Weeks-Chandler-Andersen (WCA) potential [24] (shown in Figure 2.1).

$$\begin{aligned} &V_{WCA}(r) = 4\epsilon \left[\left(\tfrac{\sigma}{r}\right)^{12} - \left(\tfrac{\sigma}{r}\right)^{6} \right] + \epsilon, && \text{if } r <= R_{cut} \\ &0, && \text{if } r > R_{cut} \end{aligned} \tag{2.7}$$

Which has all the behaviour we need for prevent beads from occupying the same space.

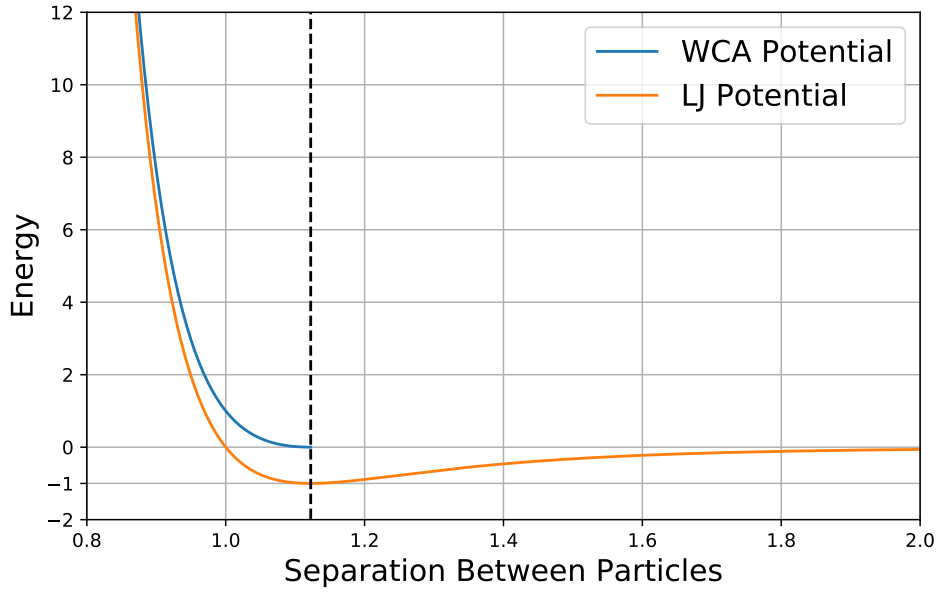

FIGURE 2.1: A plot of the LJ and WCA potentials. The LJ potential goes quickly to infinity as the separation goes approaches 0, which we want, but has an attractive component, which we do not want. The WCA potential is cut off at R_{cut}, the dotted black line, to remove the attractive component. The WCA is also shifted up by $\epsilon = 1$ so that the potential is 0 at the cutoff.

2.2.2 FENE Bonds

The objects we investigated are extended structures. Spherical beads alone are obviously inadequate for studying rods and DNA structures. In order to study these extended structures, we bonded beads together and create long chains of beads. The most basic model for bonding beads is to assume they are attached by a spring, with a potential energy of $U_{Spring} = \frac{1}{2}k(x - x_0)^2$. However, there is a significant problem with this potential; there is no maximum separation between the beads. Sufficiently large forces can push objects or other beads between the bonded beads, and disrupt our chain structure. Ideally we would like a bond which is spring-like, but has a maximum length. We use Finitely Extensible

Non-linear Elastic (FENE) bonds to accomplish this.

$$V_{FENE}(r) = -\frac{1}{2}k_{Spring}r_0^2 ln\left(1 - \left(\frac{r}{r_0}\right)^2\right) \tag{2.8}$$

Where k_{Spring} is the spring constant of the FENE bond, r_0 is the maximum extension of the bond, and r is the distance between the 2 bonded beads. This potential is illustrated in Figure 2.2.

The FENE bond alone is purely attractive. However, since the beads cannot overlap their volumes, the WCA potential should also be acting between bonded beads. By setting $k = 30/\sigma^2$ and $r_0 = 1.5\sigma$ consistent with the Kremer and Grest model [10]) the combination of the WCA potential and FENE bond acting between two beads is shown in Figure 2.2. This FENE plus WCA potential , with Kremer and Grest parameters, has a minimum at $r_{min} \approx 0.96\sigma$, which is close to 1. With a maximum separation of $r_0 = 1.5\sigma$, the maximum gap between two beads of size σ is 0.5σ, making it impossible for other beads to get between FENE bonded beads. The force applied to beads closer than r_{min} apart will is dominated by the WCA potential, and beads greater than r_{min} apart will feel a spring-like force pulling them together.

2.2.3 Angle Bonds

The objects we wish to study have an associated stiffness, which is critical to understanding their behaviour. To this end, we used a harmonic angle bond to model a stiffness on the polymer

$$V(\theta) = \frac{1}{2}k_{Angle}(\theta - \theta_0)^2 \tag{2.9}$$

Where k_{Angle} is the strength of the angle bond, θ is the angle formed by the 3 beads connected by the angle bond, and θ_0 is the resting angle of the angle bond. In all our simulations we set the resting angle of the bond to be π, to give us linear polymers.

Using both FENE bonds to keep beads together, and angle bonds to enforce a stiffness, we can create bead-spring polymers, as seen in Figure 2.3

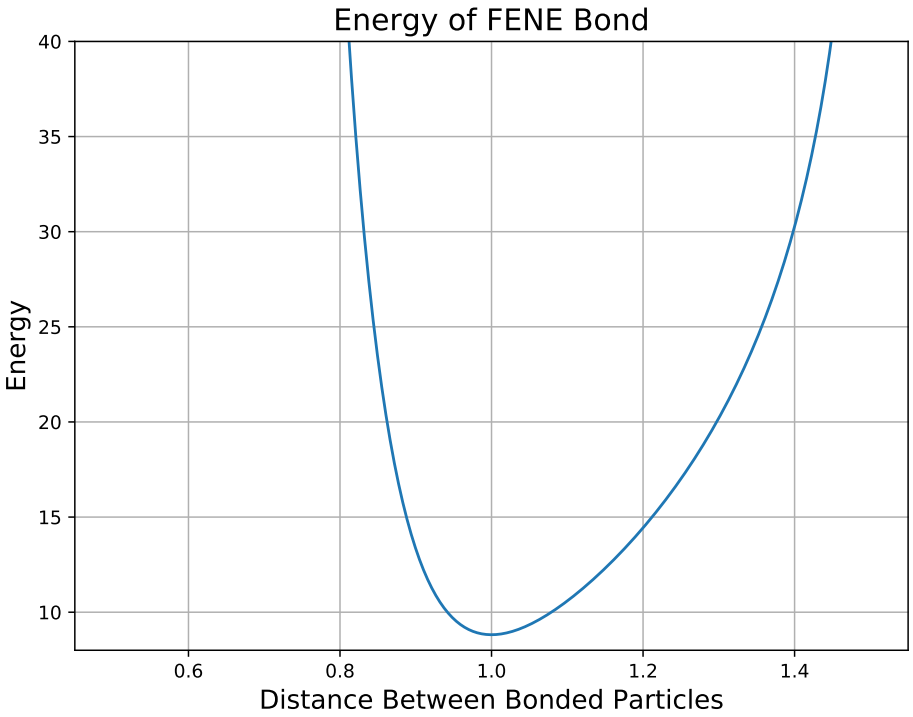

FIGURE 2.2: Potential Energy of two beads FENE bonded together, for $\sigma = 1$. The minimum is clearly at 1 and increases rapidly as you move away from 1 in either direction.

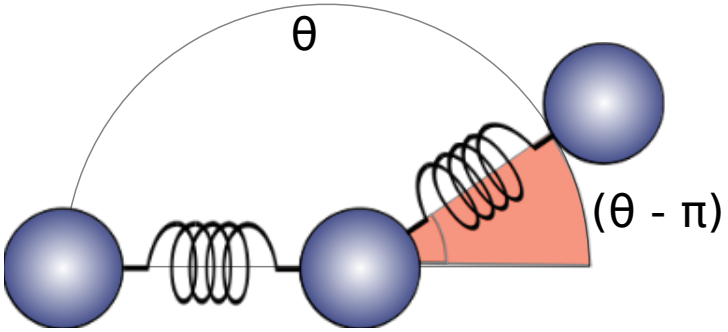

FIGURE 2.3: Using the spring-like FENE bonds to keep beads together and harmonic angle bonds to enforce stiffness across the polymer, we create these stiff bead-spring polymers. Here θ is the angle that the triple of beads makes, and π is the resting angle.

2.2.4 Worm-Like Chains

Worm-Like Chains area well studied polymer model in polymer physics. The polymer is considered a continuous thin rod, which is flexible but has some stiffness associated with it. The energy associated with bending an infinitesimal segment along the worm like chain is

$$dU = \frac{1}{2}k\left(\frac{d\theta(s)}{ds}\right)^2 \tag{2.10}$$

Where k is the bending energy and $\theta(s)$ is the direction that the chain is pointing at a point s along the chain. Note the similarity between equations 2.9 and 2.10. Equation 2.9 is effectively a discretized version of equation 2.10, if $\theta_0 = \pi$. For the worm like chain model, we know from Landau and Lifshitz (2013) [15] that

$$\langle cos\theta_{i,j}\rangle = e^{-l_{i,j}/l_p} \tag{2.11}$$

Where $\theta_{i,j}$ is the angle between the lines tangent to the chain at points i and j, $l_{i,j}$ is the length along the chain between points i and j, and l_p is the persistence length.

This equation says that the average correlation between the lines tangent to the curve ($\langle cos\theta\rangle$) decay exponentially with length, and that the characteristic length of this decay is the persistence length.

Also from Landau and Lifshitz, we know for a worm like chain.

$$l_p = \frac{k}{k_b T} \tag{2.12}$$

Where k is the bending energy, k_b is the Boltzmann constant and T is the temperature of the system. By lining up beads and FENE bonding them together, we can create freely jointed chains. If we angle bond consecutive triplets of the bonded beads, the bead-spring polymer we create will be a discretized version of a worm like chain. Equation 2.11 will hold for our chains, but the persistence

length should be proportional to the size of the beads, thus for our simulations

$$l_p = \frac{k_{Angle}\sigma}{k_b T} \tag{2.13}$$

Where σ is the diameter of the beads.

Another relevant quantity for worm-like chains is the Kuhn length [21]. The idea is that a polymer may be approximated as a freely jointed chain, with distance between the beads equal to the Kuhn length. For a worm-like chain, the Kuhn length is equal to twice the persistence length [21]. Comparing the length of a polymer to its Kuhn Length can give us a good idea of how rod-like it is. Polymers with length significantly less than the Kuhn Length are considered rod-like.

2.2.5 Walls

In some simulations, we used walls to constrain how beads can move. These walls are infinite planes. We used the WCA potential between the wall and the beads, noting that the r in the WCA potential energy was the shortest distance between the wall and the bead. Note that $R_{cut} = 2^{\frac{1}{6}}\sigma$ for the WCA potential, so the walls could only act on beads within R_{cut} of the wall.

2.2.6 Periodic Boundary Conditions

In some simulations, we had periodic boundary conditions. What this means is beads which travel through the edge of the simulations space are simply translated to the other side of the simulation. In addition, this also means that beads can interact through the edge of the simulation space. Effectively, if a compound object like a rod goes partially through the boundary, part of the object will be on one side of the box, the other part on the opposite side, but it will act identically to a compound object which does not go through the boundary.

2.3 Bundling of Rod-Like Colloids Simulation Details

2.3.1 Model Polymers

We construct linear polymers from beads such that $\sigma = 1.0\sigma_{sim}$. Each bead is placed 0.5 σ_{sim} away from the last. The WCA potential is applied between beads which are not FENE bonded together. Each pair of adjacent beads is bonded together with FENE bonds and we set the diameter of both beads to be 1. This means that beads will interact with their neighbours as though they are $\sigma_{Inner} = 0.5\sigma_{sim}$, and interact with other beads in the system as though they are $\sigma_{Outer} = 1\sigma_{sim}$. This gives us much smoother rods than we would have otherwise, as seen in Figure 2.4. The length of the rods is thus the number of beads in a rod multiplied by σ_{Inner}.

Each consecutive group of three beads is grouped into a harmonic angle bond and we set k according to the simulation. The persistence length of the rod is then equal to $\frac{k_{angle}\sigma_{Inner}}{kT} = \frac{k_{angle}}{2}$.

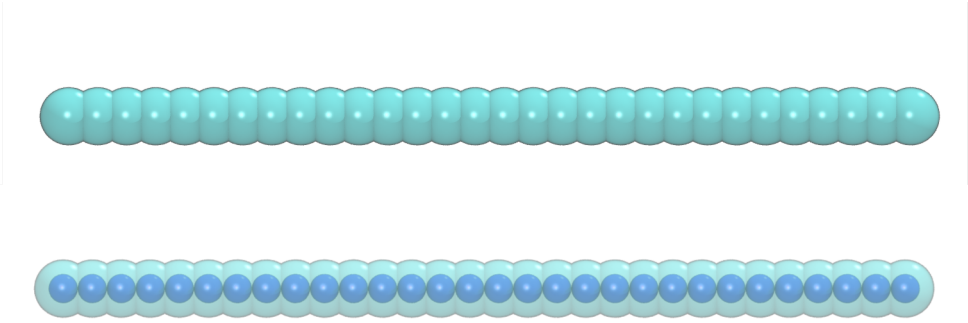

FIGURE 2.4: A Model Rod of Length 15. When interacting with other rods, the beads act as though $\sigma_{Outer} = 1$ (Top). When interacting with other beads on the rod, the beads act as though $\sigma_{Inner} = 0.5$ (Bottom)

2.3.2 Depletion Force

Like the effects of the fluid on beads, explicitly simulating depletants to cause an effective attraction is computationally unfeasible. The strength of the depletion force can be characterized by the fraction of the total volume of the system occupied by depletants, ϕ. We conduct simulations at ϕ values between 0.1 and 0.25. Given the small size of the depletant particles, reaching a ϕ value of even 0.1 can require many thousands of depletant particles. We instead use the Asakura-Oosawa [2] (AO) potential to implicitly model the depletants.

$$V_{AO} = \begin{cases} \left(\frac{R}{R_d}\right)^3 \left[1 - \frac{3}{2}\left(\frac{r}{2R}\right) + \frac{1}{2}\left(\frac{r}{2R}\right)^3\right]\phi, & \text{if } r <= 2R \\ 0, & \text{if } r > 2R \end{cases} \tag{2.14}$$

Where ϕ is the fraction of the total volume occupied by depletants, where r is the center to center distance between the two colloids, R_c is the radius of the colloid, R_d is the radius of the depletant, and $R = R_c + R_d$, which is to say it is the sum of the radii of the colliod and depletant. Note that the force cuts off at $r = 2R = 2(R_d + R_c)$, which is the distance at which a depletant particle can fit between the two colloids (Figure 2.5).

The parameter we vary in our simulations is ϕ, the depletant fraction. Our simulations take our colloids to have a radius of 0.5 σ_{sim}, our depletants to have a radius of 0.1 σ_{sim}, and we vary the amount of depletants in the system by changing ϕ. Note that the AO potential is linear in ϕ. This is because the AO potential assumes the depletants do not interact with one another, like an ideal gas. While this approximation might not be ideal at the depletant fractions we have simulated (0.05 - 0.25), we had much more success using the simple AO potential than more complicated potentials that took into account interactions between depletants.

The size of the depletants compared to the colloid has multiple effects on the depletion force. The magnitude of the depletion force is heavily dependent on $\frac{R}{R_d} = \frac{R_c+R_d}{R_d}$, the ratio of the radius of the depletants to the radius of colloids + depletants. Lowering the size of the depletant causes the magnitude of the depletion force to become much stronger. In addition, as the size of the depletant

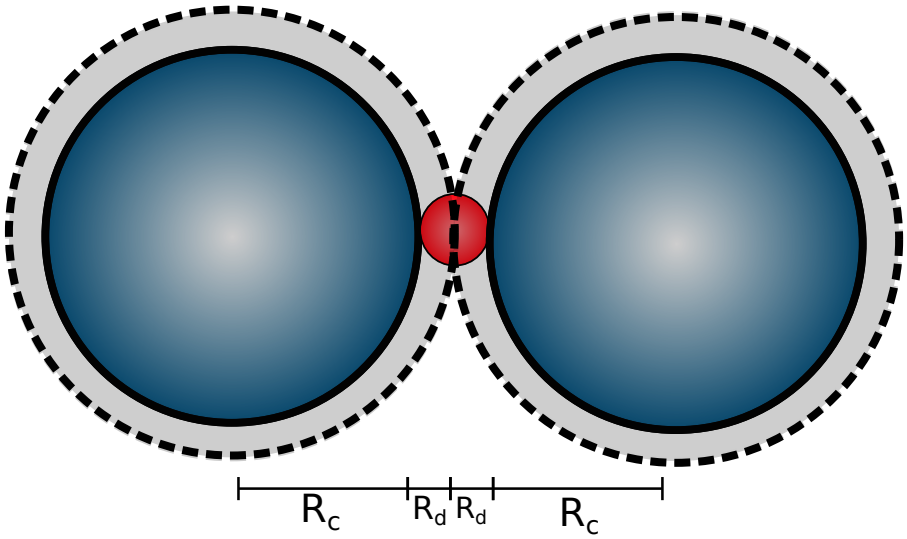

FIGURE 2.5: Schematic of two colloids at the cutoff distance for the AO potential. At $R_{cut} = 2(R_d + R_c)$, there exists enough space for a depeletant to fit between the colloids. In addition, R_{cut} is the distance at which the excluded volumes are no longer overlapped.

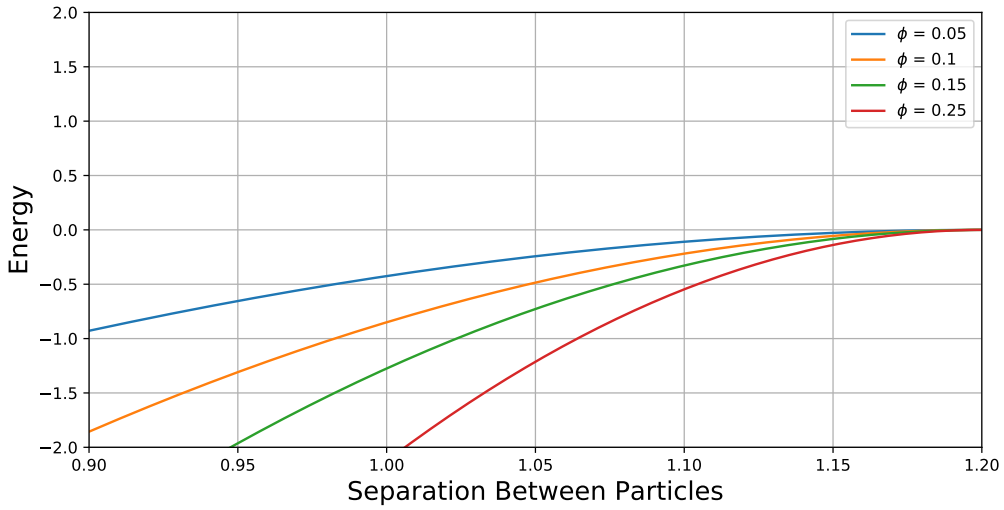

FIGURE 2.6: Energy of the Asakura-Oosawa potential as function of bead separation. This potential is monotonically increasing as r increases.

decreases, the maximum range over which the force acts, $2R = 2(R_d + R_c)$, decreases. Since changing the depletant or colloid size affects the potential and force in significantly more complicated ways than changing the volume fraction of depletants, we just set a given radius of depletants ($R_d = 0.1\sigma_{sim}$) and colloids ($R_c = 0.5\sigma_{sim}$) and varied the volume fraction to change the strength of the depletion force.

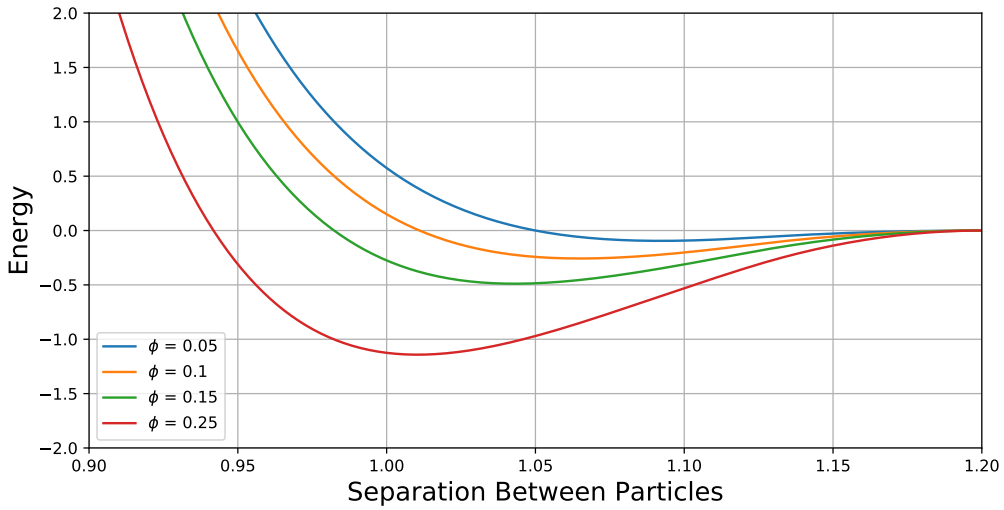

FIGURE 2.7: Energy of the Asakura-Oosawa potential plus the WCA potenial. This is the energy between two unbonded beads in our simulations. Adding the WCA potential causes the total potential to increase rapidly as the separation decreases. The interaction between the purely repulsive WCA potential and the purely attractive AO potential yields a potential energy well at all values of ϕ we investigated.

Figure 2.6 shows the energy associated with the Depletion Force alone for our chosen colloids and depletants. We can see that the AO potential is monotonically increasing with r until the cutoff at $2R = 2(R_d + R_c) = 1.2\sigma_{sim}$. This means our depletion force is a purely attractive force. However, in our simulations, beads with depletion forces acting between them will also have the WCA potential acting between them. Figure 2.7 shows the energy of the Depletion Force and WCA potential added together. The WCA potential is

purely repulsive and the AO potential is purely attractive. When we add them together, we get a potential energy well around $r = 2R_c$. As r approaches 0, the WCA potential is significantly stronger than the AO potential, so we retain a fairly hard shell for our beads.

2.3.3 Bundling Analysis

In order to describe the degree of bundling in our system of rods, we use the fraction of rods which are not in a bundle. There are two conditions for a rod to be considered bundled with another rod. First, the rods must be within $2(R_d + R_c)$ of one another. This just means that the depletion force needs to acting between the 2 rods. However, rods which are simply close to another are not necessarily bundled. Rods which are close but not aligned are not considered bundled (Figure 2.8). Thus, the end to end vectors of both rods must also be within 15 degrees of being parallel.

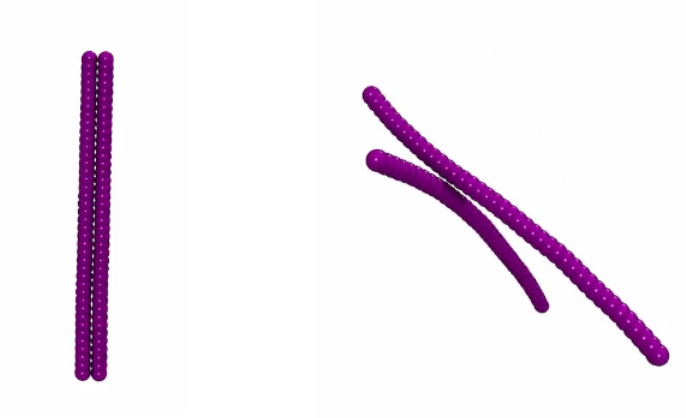

FIGURE 2.8: On the left are two rods we consider bundled. They are close enough together, and they are parallel. On the right are two rods which are close enough together, but do not satisfy the angle condition, and so we do not consider them bundled together.

2.3.4 Simulation Setup

We ran two kinds of simulations to analyze the behaviour of rod like colloids. The first were bundling simulations, where many rods would begin in an unbundled state, and we would apply the depletion force between them and observe the behaviour of the system. The second were two rod bundle separation simulations, where we initialized two rods in side to side contact, and found the average time it took for those rods to separate from one another.

Bundling Simulations

In bundling simulations, we initialized a number of rods rods in a cubic simulation box, 60 σ_{sim} in height, with periodic boundary conditions. We initialize the rods parallel with one another in a grid-like structure. The simulation is run in 3 phases. We simulate the system, without depletants in order to equillibrate the system. This is the equillibration phase. Though the rods are initialized in the same direction and in a grid, in this phase their position and orientation will be randomized. Then we simulate the system under the effects of depletants. The majority of the bundling should take place during this time, known as the main simulation phase. Finally the system was simulated for an additional time period, recording the average number of unbundled rods in the system over this time frame. This is the data collection phase.

Two Rod Bundle Simulations

The other type of simulations we ran looked to quantify the behaviour of the system in terms of the behaviour of the simplest bundle, the two rod bundle. We simulate a system of two rods initialized in side-to-side contact. We simulate these rods for $5 \cdot 10^3$ τ and record how long it takes for the two rod bundle to break apart. We consider the rods to have broken apart when the rods have moved far enough away from one another that the depletion force is no longer acting between them (when all beads of one rod are more than $2(R_d + R_c)$ from all the beads of the other rod). The time for a two rod bundle to break apart is the separation time of the two rod bundle. We also record the energy associated

with the AO and LJ potentials acting between each pair of rods until the two rods break apart. We record this energy every 0.5 τ. This simulation procedure is shown in Figure 2.9

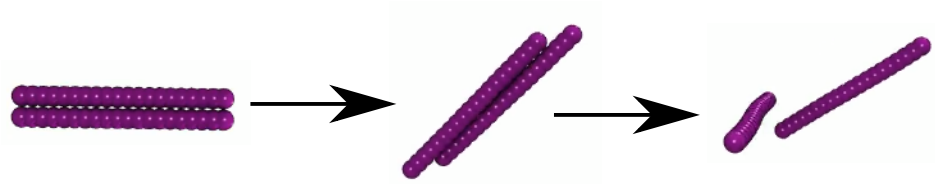

FIGURE 2.9: Pictures from simulations of two rod bundles. We initialize the rods in side to side contact (On the left). We simulate the bundle until it breaks apart.

If the bundle does not break apart within the $5 \cdot 10^3$ τ simulation time, we consider the separation time of the two rod bundle to be $5 \cdot 10^3$ τ. We have chosen our parameters such that less than 5 % of simulations with any combination of parameters hit the wall time.

2.4 Triple Helix Bundle Simulation Details

2.4.1 Model Polymers

We construct linear polymers from beads such that $\sigma = 1.0$. Each bead is placed 1 σ_{sim} away from the last. Each pair of adjacent beads is bonded together with FENE bonds. Each consecutive group of three beads is grouped into a harmonic angle bond with k_{angle} dependent on the polymer we are modelling. The WCA potential is applied between beads which are not FENE bonded together. This basic linear polymer model can be used to create more complicated structures. We can also use it to model dsDNA, or to model 3HB very roughly.

2.4.2 Ribbon Model

Our initial model of 3HB was the Ribbon Model. In the ribbon model, we essentially stick 3 strands of dsDNA together side-by-side. We create three linear polymers of 100 beads each, with $k_{angle} = 25$. We lay them side by side, and

FENE bond each adjacent bead together. The result is shown in Figure 2.10. In simulations where we use the ribbon model, we set $\sigma_{sim} = 2nm$, about 6 base pairs in length. Thus, each linear polymer has a persistence length of 50 nm, which is the persistence length of dsDNA. We initially expected this to give our ribbon model a persistence length of 3 times dsDNA persistence length.

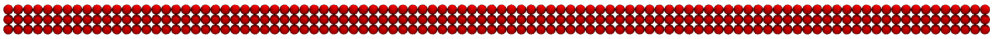

FIGURE 2.10: A Picture of our Ribbon Model of the Triple Helix Bundle. This model is long and flat; shaped like a ribbon.

2.4.3 Pore Geometry

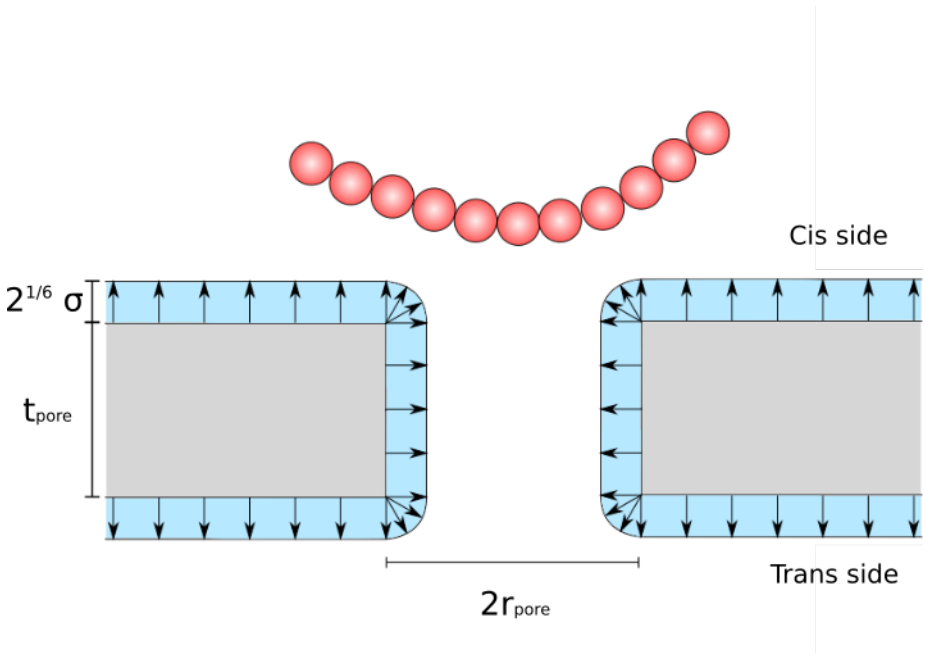

FIGURE 2.11: Schematic of pore. The grey area is the membrane, and beads cannot occupy this region due to the walls. If the center of a bead is in the blue region, the WCA potential will push the beads away from the wall.

We wanted to run simulations of polymers translocating through a pore. To this end, we needed to define forces which stop the polymer from translocating at any point other than the pore. We created two walls, a distance t_{pore} apart, which we termed the membrane. Then we created a cylindrical gap in the membrane, with a radius r_{pore}, which we termed the pore. Then, we applied the WCA potential between the pore structure and the beads, with the radius being the shortest distance between the membrane and the beads. We considered the space above the membrane to be the cis side of the pore, and the space below the membrane to be the trans side of the pore. This set up is shown in Figure 2.11.

In some simulations, we set the thickness of the pore to be 0. In these cases, there is just a single wall with a circular gap.

2.4.4 Electric Field

To drive the polymer across the pore, we needed to implement an electric field for the pore. We use the electric field from Farahpour [8] (Figure 2.12). The field uses oblate spheroidal coordinates (μ, ν, ϕ), which map to Cartesian coordinates as follows.

$$\mu = cosh^{-1}\left(\frac{\sqrt{(\sqrt{x^2+y^2}+a)^2+z^2}+\sqrt{(\sqrt{x^2+y^2}-a)^2+z^2}}{2a}\right) \tag{2.15}$$

$$\nu = cos^{-1}\left(\frac{\sqrt{(\sqrt{x^2+y^2}+a)^2+z^2}-\sqrt{(\sqrt{x^2+y^2}-a)^2+z^2}}{2a}\right) \tag{2.16}$$

$$\phi = tan^{-1}\left(\frac{y}{x}\right) \tag{2.17}$$

Where a is the position of the foci of the ellipses. In our simulations, this will always be set to the radius of the pore.

In oblate spheroidal coordinates, the electric field outside the pore is

$$E = -\frac{V_{out}\hat{\mu}}{a\pi cosh(\mu)\sqrt{sinh^2(\mu) + sin^2(\nu)}} \tag{2.18}$$

Inside the pore, we modelled the field as being constant and pointing in the $\hat{z}$ direction. Thus, the field inside the pore, in Cartesian coordinates, is

$$E = -\frac{\Delta V_{pore}}{t_{pore}}\hat{z} \tag{2.19}$$

Where t_{pore} is the thickness of the pore, V_{out} is the voltage outside the pore, and ΔV_{pore} is the drop in voltage going from the cis side of the pore to the trans side of the pore. These are related to the total voltage drop of the system, V_0, as follows.

$$\Delta V_{pore} = \frac{V_0 t_{pore}}{a\pi + t_{pore}} \tag{2.20}$$

$$V_0 = \Delta V_{pore} + V_{out} \tag{2.21}$$

In our simulations, each bead has a charge of 1 charge unit, and thus the electric field is also the force felt on a bead in simulation.

$$\vec{F_{electric}} = q\vec{E} = \vec{E} \tag{2.22}$$

This field pulls the polymers close to the pore from the cis side of the pore, and also drives them through the pore, to the trans side. The field is very strong at the pore, and far from the pore decays as r^{-2}, where r is the distance from the pore. In simulations, we will generally vary V_0, which we will sometimes call the simulation voltage.

Equations 2.21 and 2.22 effectively break the potential difference in the system into two parts. The potential difference of the pore, V_{pore}, and the potential difference outside the pore, V_{out}. Increasing the radius and thickness of the pore will increase V_{pore} and thus lower V_{out} at a constant simulation voltage.

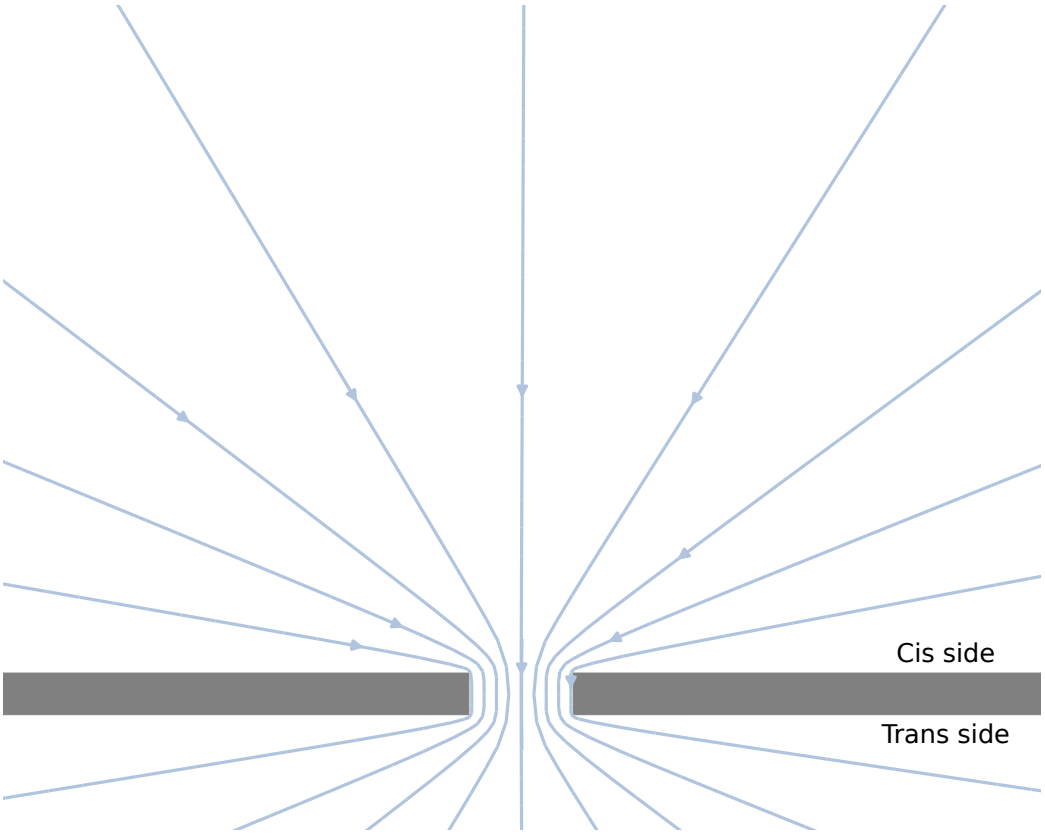

FIGURE 2.12: Cross section of pore and Electric field. Inside the pore, the field is constant. A polymer will be drawn from the cis side, through the pore and onto the trans side by the electric field.

2.4.5 Equilibrated Configurations

In some simulations, we require polymers to start in a random configuration. To do so, we run a simulation with just the polymer in space. We record the polymer's configuration at regular intervals, such that there is no correlation between the recorded polymers. We consider these configurations to be equilibrated, and we use them as starting configurations of polymers in simulations where we initialize the polymers far from the pore.

2.4.6 Defects

We introduce defects into the polymer in some simulations. To induce a defect on a certain bead of a polymer, we remove two adjacent angle bonds acting on that bead, as seen in Figure 2.13. Taking off two angle bonds should allow the polymer to rotate freely around the defect.

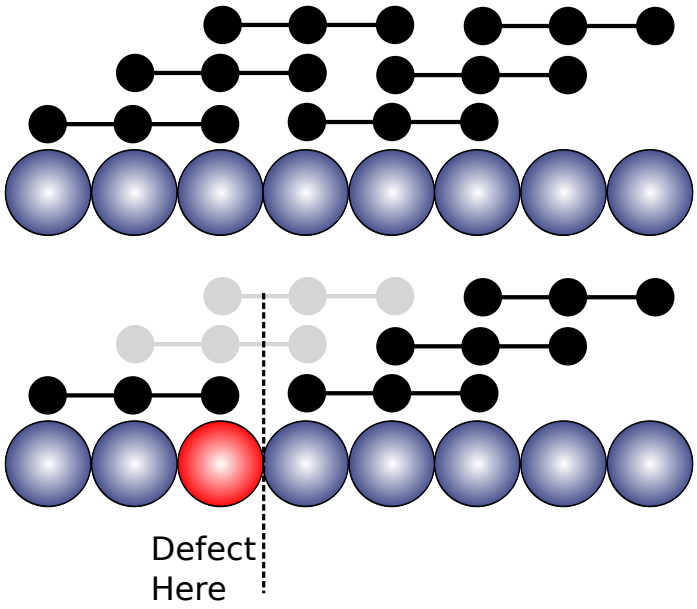

FIGURE 2.13: Schematics of defects, with the large beads being the beads along the polymer and each connected triple of dots represents an angle bond connecting the three beads below it. Defects are located at the red beads. Above is a non-defective polymer, while below is a polymer where we have induced a defect. In the below example. we can see there are no angle bonds connecting the beads before and after the defect.

2.4.7 Simulation Setup

We ran two types of simulations of polymers close to a nanopore. The first type were capture and translocation simulations, where the polymer was initialized far from the pore, and would be pulled towards the pore by the electric field, and eventually translocate through the pore. The other type of simulation were

lateral diffusion simulations, where the polymer was initialized with its center above the pore, and we recorded how the polymer moved above the pore.

Capture and Translocation Simulations

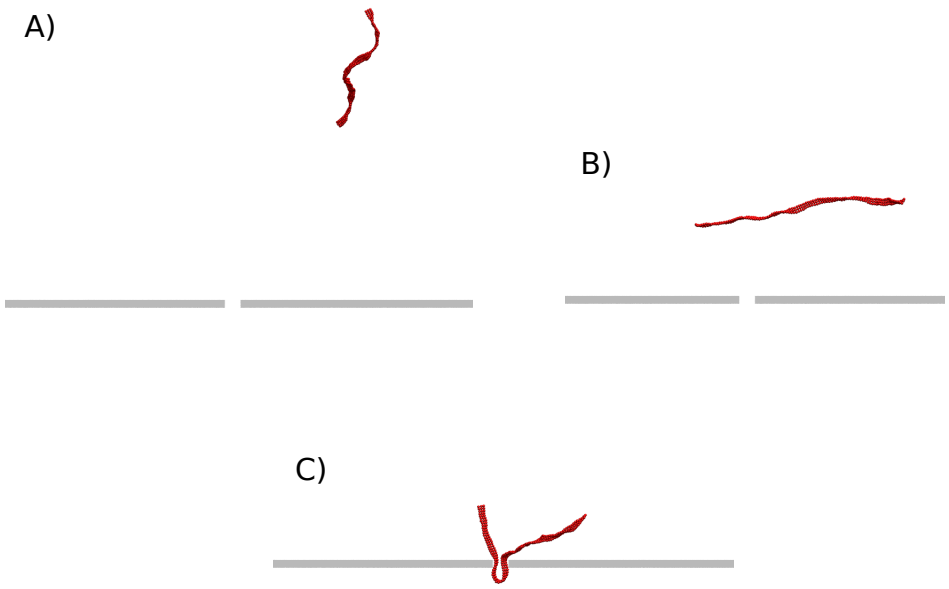

FIGURE 2.14: Simulation process for the capture and translocation simulations. A) The polymer is initialized in an equilibrium configuration far from the pore. B) The polymer diffuses around the simulation space, while being pulled towards the pore. C) Once the polymer is pulled close to the pore, it is pulled through. We record the the point at which the polymer translocates through the pore.

In Capture and Translocation Simulations, we simulated a pore with a given radius r_{pore}, and a given thickness t_{pore}. We also applied a potential difference of V_0, the simulation voltage, across the pore. We then initialized polymers in a random configuration, such that the center of mass of the polymer was $100\sigma_{sim}$ away from the center of the pore. These polymers were equally likely to be initialized anywhere on hemisphere of radius 100 σ_{sim} above the pore, however if a polymer was initialized inside the membrane, we would reinitialize it. These polymers would be drawn close to the pore and eventually translocate through, as

shown in Figure 2.14. When a piece of the polymer was halfway through the pore, we recorded the first bead along the polymer to cross the halfway the pore. We considered this to be the translocating monomer. Finally, once the polymer was entirely through the pore, we considered the event finished, and reinitialized the polymer.

Lateral Diffusion Simulations

In our lateral diffusion simulations, we initialized a polymer $20\sigma_{sim}$ above the pore with radius r_{pore} and thickness t_{pore}, with its center above the pore. We applied a potential difference of V_0, the simulation voltage, across the pore. The electric field would quickly pull the polymer towards the pore, and once the polymer is at the pore we recorded the monomer which was furthest into the pore. The location of this monomer along the length of the ribbon is our lateral diffusion coordinate. If the polymer translocates, such as by diffusing such that an end is over the pore and threading through, we reinitialize it. We simulate this system for 30000τ.

2.5 Units

HOOMD-Blue has base units of length, energy, and mass, and derives all its other units from these units. In our simulations, we set the mass of every bead to equal 1 simulation mass unit, and we set the temperature such that $kT = 1$ simulation energy unit. The characteristic length scale, henceforth σ_{sim}, was dependent on the simulation.

In the case of rod-like colloids, we did not match these to experimental parameters, as we wanted to work with generic rods. However, we can match our simulation values to Tobacco Mosaic Virus, a well known rod-like virus, in order to get a rough idea of the time scale of our simulations. From Bruckman, M. A., & Steinmetz, N. F. (2014) [5], we know that the molecular weight of TMV is 3.94×10^7 Da, or 6.59×10^{-20} kg. The length of TMV is 300 nm, and its width is 18 nm, and thus the ratio of length to width is $16.67 \approx 17$. In our simulations, this would be equivalent to a length 17 rod, which has 34 particles in it. Thus $\sigma_{sim} = 18$ nm, the width of TMV, and the mass of one particle would be the

molecular weight divided by 34, or 1.94×10^{-21} kg. Given a temperature of 300 K, our energy unit will be $4.14x10^{-21}$ J. Length, mass, and energy can be related to time as

$$[time] = \frac{[length][mass]^{\frac{1}{2}}}{[energy]^{\frac{1}{2}}} \tag{2.23}$$

and thus our time unit τ in this case would be 1.23×10^{-8} s, or about 12 ns. We expect simulations of other rod-like colloids to be on this timescale.

In the case of 3HB, we worked with a model of 3HB, where each bead represented 6 base pairs of dsDNA, in addition to more generic models to test certain phenomena. Given each base pair should have a mass of 1.10×10^{-24} kg and a length of 0.34 nm, our length unit is 2 nm, and our mass unit is 6.60×10^{-24} kg. Additionally we set the temperature to be 300 K, and thus our energy unit should be 4.14×10^{-21} J. Relating energy, length, and mass to time as before our time unit τ is roughly 7.99×10^{-11} s, or roughly 80 ps.

Chapter 3

Bundling of Rod-Like Colloids Results

Previous work by our lab investigated the behaviour of discs with the depletion force acting between them and how they form rouleaux. Our goal for these simulations was to explore how rod-like objects form larger structures when depletion forces is acting between them. This study of rod-like structures is of interest in certain biological systems. For example, rod-like Actin filaments inside cells can be forced into bundles by depletion forces [22]. The environment inside of a cell has various macromolecules which can act as depletants. Understanding the self assembly of rod-like objects acting under depletion forces can give us new tools to separate mixtures of rods.

3.1 Bundling Behaviour

Our first objective was simply to simulate colloidal rods with the depletion force acting between them, and obsereve how bundling occurs. We initialized 40 rods in a cubic simulation box, 60 σ_{sim} in height, with periodic boundary conditions. We ran bundling simulations of 40 rods, with an equilibration phase of length $5 \cdot 10^2\tau$, a main simulation phase of $3 \cdot 10^3\tau$, and a data collection phase of $5 \cdot 10^2\tau$. These simulations were run for rods of persistence length 1000 σ_{sim}, over various lengths. 10 simulations were run for each rod length and ϕ value.

Figure 3.1 shows the average number of unbundled rods from these simulations. At low values of ϕ, the rods are primarily unbundled. At high values

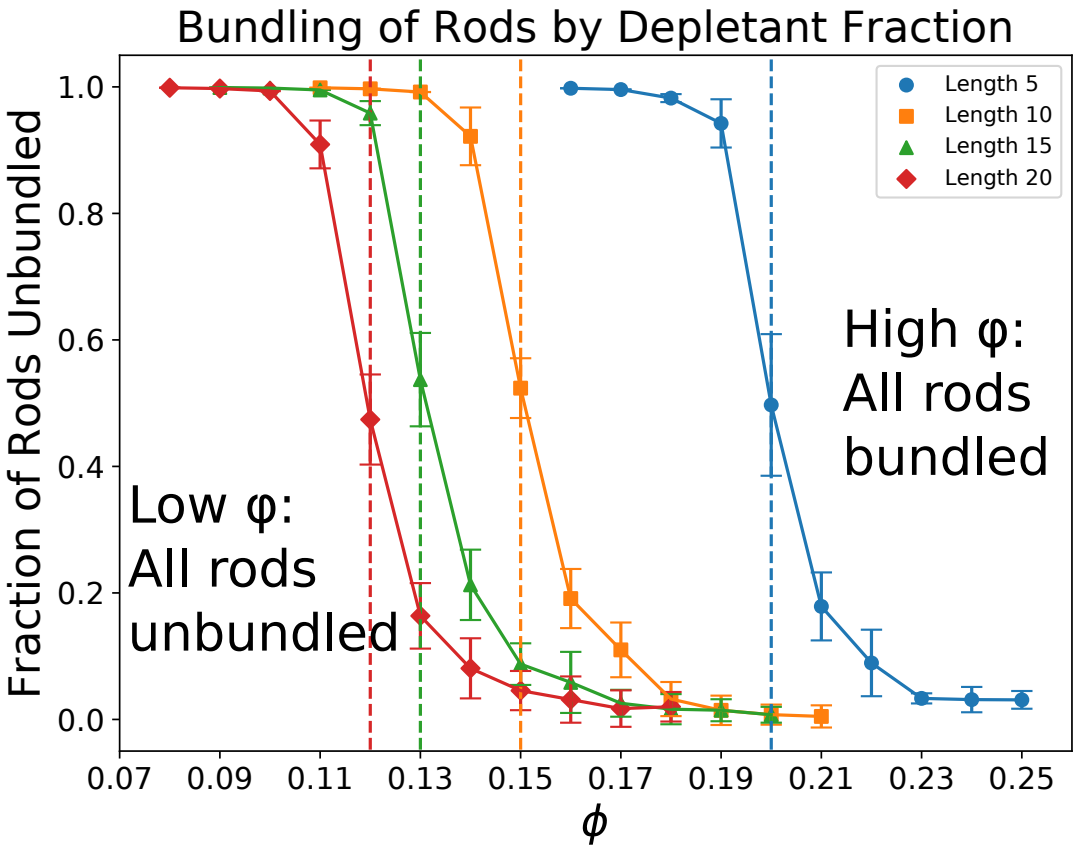

FIGURE 3.1: Fraction of rods unbundled as a function of ϕ. A transition region, between almost entirely unbundled and almost entirely bundled is observed for each length. We designate the edge of the bundled region to be ϕ_{crit}, shown as a dotted line for each rod length. Error bars are twice the standard error.

of ϕ, nearly all the rods are bundled. Pictures from simulations of both of these regions can be found in Figure 3.3. Between these two regions there is a transition region. The value of ϕ where less than 60 % of the rods are unbundled we designate the critical depletant fraction or ϕ_{Crit}. At this level of bundling, a significant portion of the system is bundled, with larger bundles beginning to appear. At these values of ϕ, the system would continue to form bundles over a longer simulation time and thus we consider these ϕ values to be the lowest values

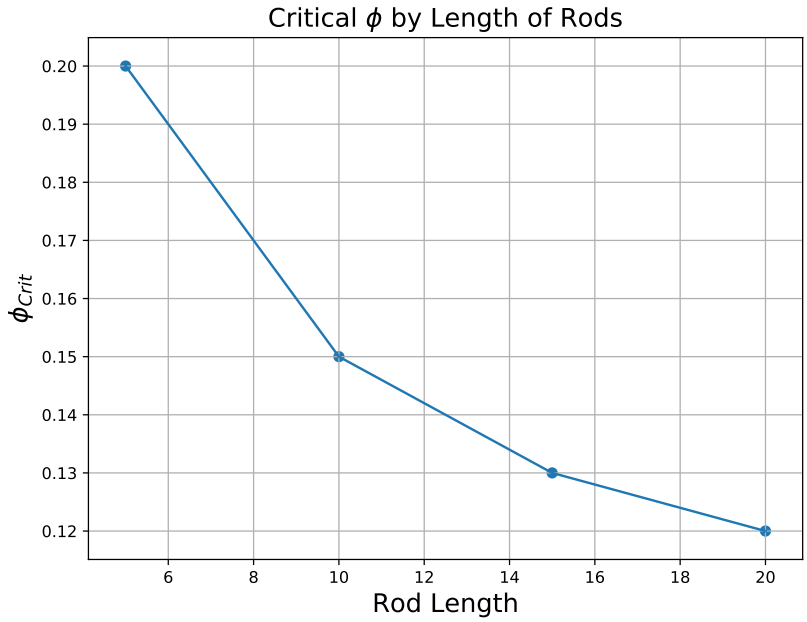

FIGURE 3.2: Plot of the critical depletant fraction by rod length. The longer rods have a lower ϕ_{crit} due to their larger excluded volume.

where bundling occurs. ϕ_{Crit} for each rod length is shown as a dotted line on Figure 3.1, and is shown in Figure 3.2. The value of ϕ_{Crit} decreases with the length of the rods. This result is sensible, as the longer rods have greater excluded volume and thus require a lower depletant fraction for them to bundle.

In our lab's previous work on the self-assembly of discs via the depletion force, it was found that, at a critical depletant fraction, the discs would form into rouleaux. As the depletant fraction increased further, the discs would begin to form more amorphous structures. In the simulations of rods outlined in this section, this behaviour is not seen at the depletant fractions studied; increasing the depletant fraction past the critical depletant fraction does not change the structure of the bundles.

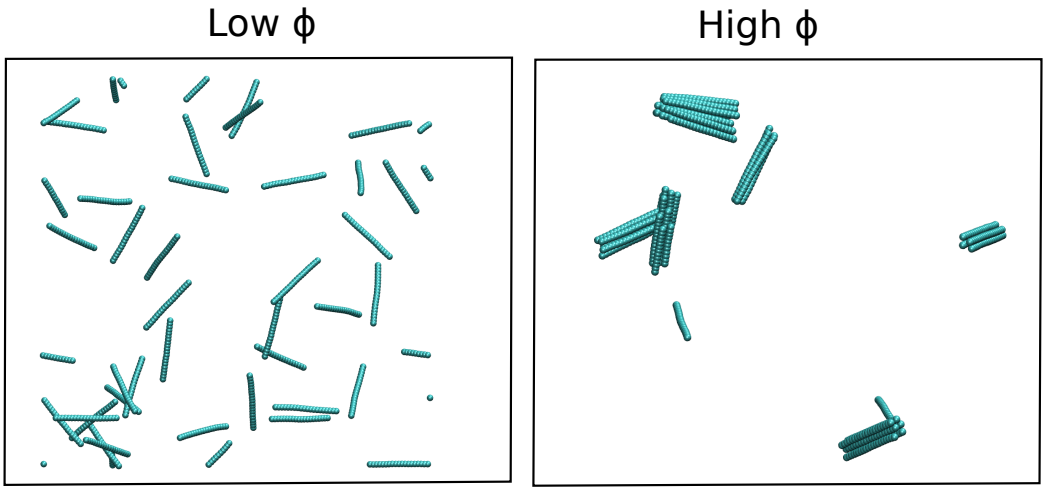

FIGURE 3.3: Pictures from simulations of rods length 10. On the left is a system simulated at $\phi = 0.12$, which remains primarily unbundled. On the right is a system simulated at $\phi = 0.18$, where the rods are all bundled.

3.2 Analysis of Bundling

The most basic and easy to analyze bundle is a bundle of two rods. Figure 3.4 shows both the cross section and the side view of a two rod bundle. The side view is typical of two rod bundles; they are mostly in side to side contact with the rods being only a little offset lengthwise. The cross sectional top view shows the excluded volume as well as the rods. We can see that the 2 rod bundle overlaps the excluded volumes at a single point. Note that the attractive entropic force of the depletion force occurs because of this overlapped excluded volume.

With larger bundles, it is observed that the overlap of excluded volumes increases dramatically. Figure 3.5 shows a typical three rod bundle, and a robust seven rod bundle. The addition of a third rod to the bundle adds two overlapped regions. This significantly increases the energy associated with the depletion forces binding the rods together. The seven rod bundle shown is even stronger. Each of the six rods on the outside of the bundle has three overlaps of excluded volume with other rods in the bundle, while the rod on the inside has six overlaps. With a two rod bundle having one overlap between two rods, a three rod bundle having three overlaps between three rods and a seven rod bundle

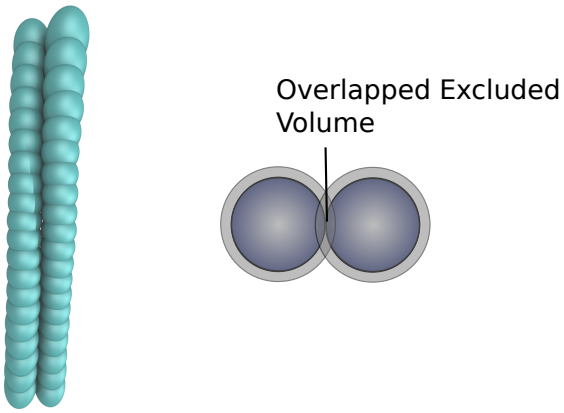

FIGURE 3.4: On the left is a picture of a two rod bundle from the simulations. Being in side to side contact maximizes the overlap volume. If one of the rods slides away from the other, the overlapping excluded volume decreases. On the right is a picture of a two rod bundle from the top, with the excluded volume shown.

having twelve overlaps between seven rods, it can be concluded that the stability of the bundles increases with the size of the bundle.

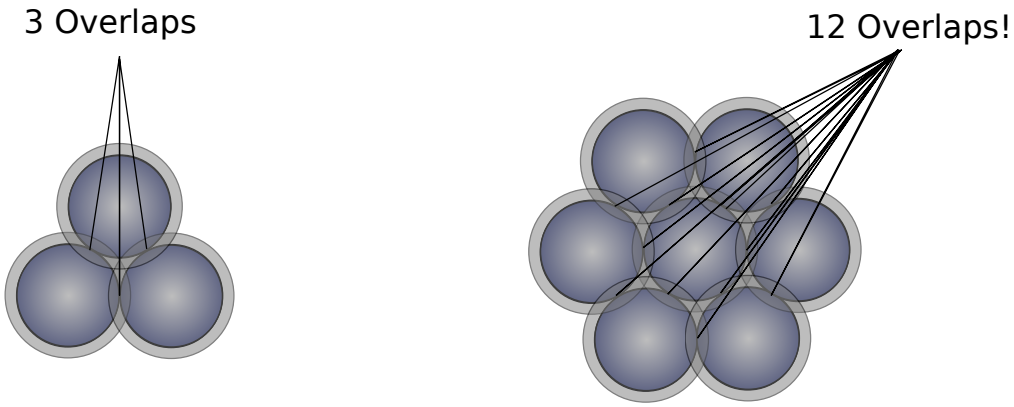

FIGURE 3.5: Pictures of a three rod bundle and seven rod bundle, from the top. The excluded volume is shown. Compared to the 2 rod bundle shown in 3.4, the three rod bundle has much more overlapped volume, even if you average the overlapped volume over the number of rods. The seven rod bundle has even more overlapped volume.

These observations have a couple of implications. One is that in our simulations, there is no upper bound on the size of these bundles. The only

limiting factor on how these bundles grow once they are large enough is the rate at which new rods will come into contact with the correct orientation. Another implication is the importance of the two rod bundle. Since this is the least stable stage of bundle formation, as well as the simplest bundle to analyze, we use simulations of two rod bundles to provide additional insight into the system. When a two rod bundle forms it will either dissociate back in individual rods, or it survives long enough for an additional rod to come in contact with the bundle and increase the bundle's stability. The two factors here are the rate at which the two rod bundle breaks apart, and the rate at which new rods come into contact with the bundle. The rate at which the bundles break apart is what we will discuss later on, and the rate at which new rods come into contact with the bundle depends on the rate at which the rods diffuse and the number of rods in the system. For bundle formation to be prevented, the rate at which two rod bundles break apart must be greater than the rate at which new rods stick to the bundle. In this work, we focus on the former, and assume that the rate at which rods find one another is constant.

3.3 Analysis of Two Rod Bundles

To simplify our system, we can analyze bundle formation by analyzing how long a two rod bundle can survive, on the basis that in a system where two rod bundles cannot survive long enough for it to come into contact with a third rod, a large bundle is extremely unlikely to form.

We ran two rod bundle simulations for rods between lengths 5 and 20, and for rods with persistence lengths between 100 σ_{sim} and 1000 σ_{sim}. For each combination of length and persistence length, simulations were performed at a variety of depletant fractions. For each combination rod length, persistence length and depletant fraction, we simulated 200 bundles.

Figure 3.6 shows the results of our simulations for rods of length 10. For a single particle in a potential energy well undergoing thermal fluctuations, we expect this to be a Kramers' escape problem [14], and that the MFPT should go

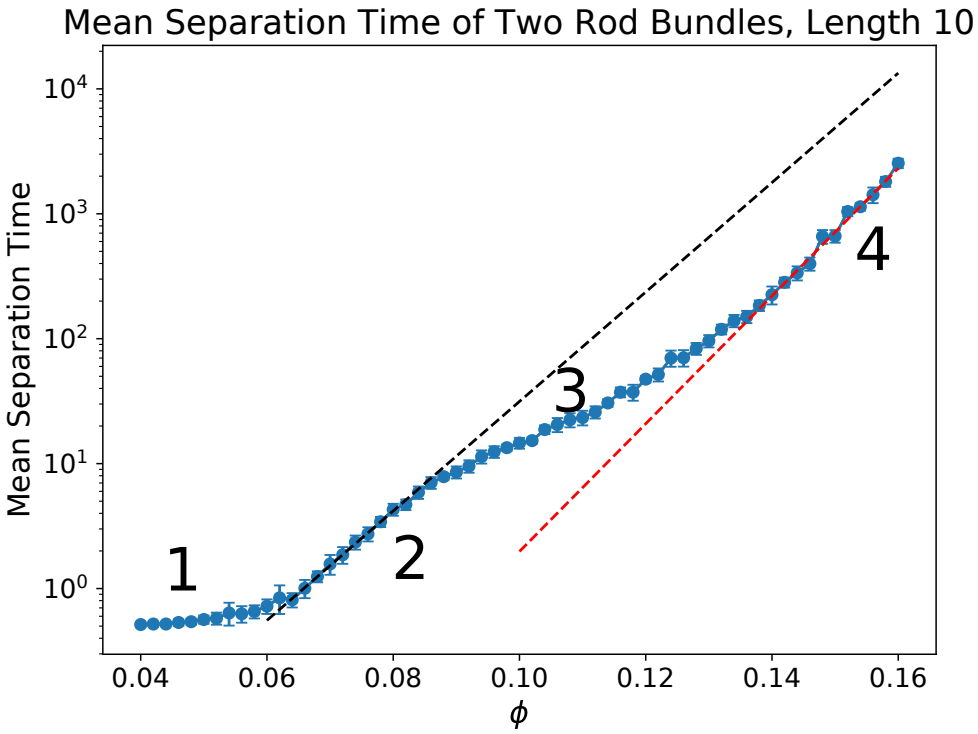

FIGURE 3.6: Plot of the mean separation time of two rod bundles for rods of length 10 and persistence length 1000 σ_{sim}. We see 4 distinct regions in the growth of the mean separation time. Region 1: Diffusion dominated, mean separation time is constant. Region 2: Depletion force becomes significant enough to inhibit diffusion, and the mean separation time experiences exponential growth. Region 3: Region of inhibited mean separation time growth. We assume that this region is due to the shape of the rods. Region 4: Mean separation time slope becomes similar to that of Region 2 again.The dotted black line is exponential function fitted to the region between 0.062 and 0.08, roughly region 2. The dotted red line is exponential function fitted to the region between 0.130 and 0.160, roughly region 4. Error bars are two times standard error.

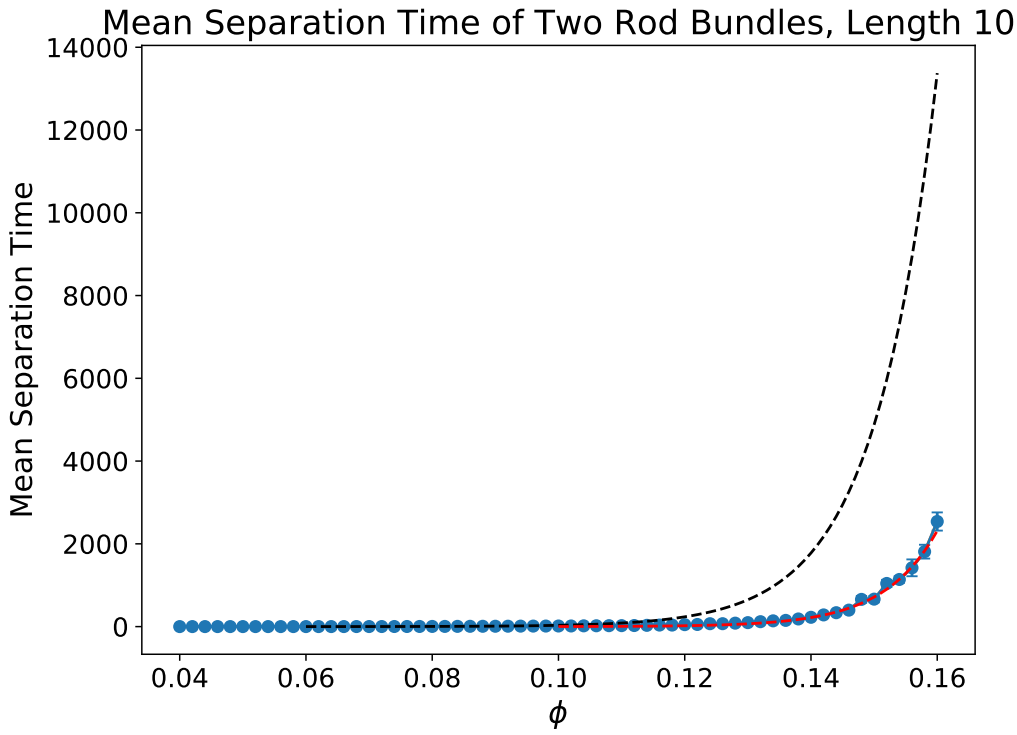

FIGURE 3.7: Plot of the mean separation time two rod bundles for rods of length 10 and persistence length 1000 σ_{sim}. As compared to Figure 3.6, this plot is linear instead of logarithmic in y. The dotted lines correspond to the fitted lines from Figure 3.6. Here we can see that the effect of region 3 has a large effect on the mean separation time of two rod bundles, even as the system moves into region 4.

as

$$MFPT = Ae^{\frac{\Delta U}{kT}} \tag{3.1}$$

with A being an inverse attempt frequency, ΔU being the energy barrier, k_b is the Boltzmann constant and T is the temperature. The MFPT of a particle escaping an energy well is analogous to the mean separation time of a two rod bundle. If we take the natural logarithm of this and note that in our simulations, $kT = 1$, we get

$$lnMFPT = lnA + \Delta U \tag{3.2}$$

Which is to say the natural logarithm of the MFPT should be linear with respect to the energy barrier, assuming A does not change as we change the energy barrier. Since our AO potential is linear with respect to ϕ, we expect ΔU to be roughly linear with ϕ as well. Thus, we should see a straight line on a log plot of the mean separation time.

Figure 3.6 shows significantly more complicated behaviour in the mean separation time. We see four distinct regions. Region 1 is at the very low depletant fractions. At low depletant fractions, the mean separation time is constant. This is because the energy of the thermal fluctuations of the system are much greater than the energy associated with the depletion force, and the rods simply diffuse apart. This diffusion should be independent of ϕ, as thermal fluctuations dominate the system. At around $\phi = 0.06$, we enter Region 2, where the energy of the depletion force approaches the energy of the thermal fluctuations. We begin to see the increase in the mean separation time we would expect from a Kramers' escape process. At around $\phi = 0.09$, the mean separation time deviates from what we would expect, and we consider this Region 3. The black dotted line on Figure 3.6 is a exponential function fitted to the region between $\phi = 0.063$ and $\phi = 0.08$, and this is how we expect the mean separation time of a particle to increase. However the increase is notably slower between $\phi = 0.09$ and $\phi = 0.13$. After the about $\phi = 0.13$, the mean separation time we found in the simulation is roughly parallel to the black dotted line. The red dotted line is fitted in the same way as the black dotted line, except it is fitted to the region between $\phi = 0.13$, and $\phi = 0.16$. We see that the red dotted line and the black dotted line are close to parallel, and thus we consider the region between $\phi = 0.13$, and $\phi = 0.16$ to be Region 4.

Figure 3.7 shows the same data plotted on a linear plot. Here we can see the effect of region 3 on the mean separation time of a particle quite clearly. Our expectation is that without region 3, the separation time would behave as the dotted black line. However, we can see the mean separation time is significantly suppressed in regions 3 and 4.

We ran a similar simulation set up for 2 beads breaking apart, shown in Figure 3.8. Due to our ratio of the size of the colloids and depletants, these simulations

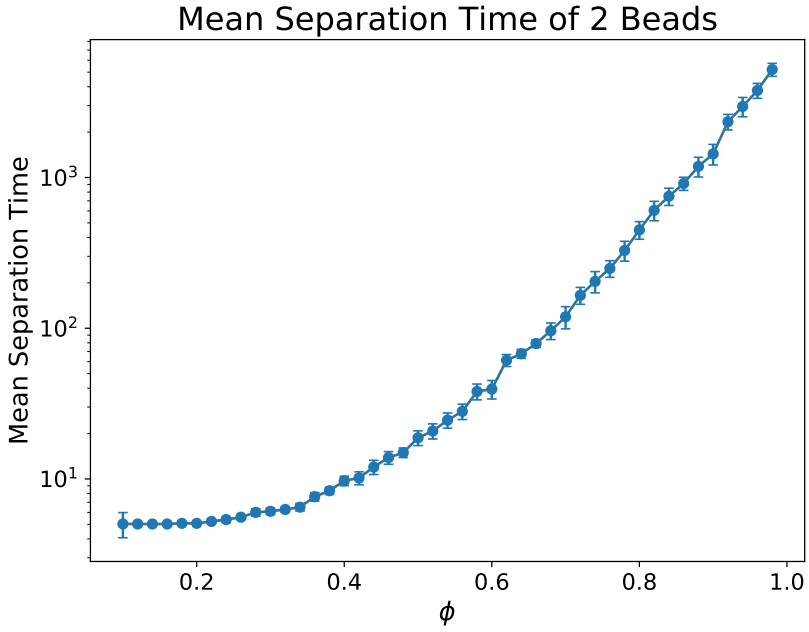

FIGURE 3.8: Plot of the mean separation time of 2 beads breaking apart. We see the diffusive region at low ϕ, and we see growth region at the higher values of ϕ which is not strictly linear, but has an increasing slope. We do not see regions 3 or 4 for a particle. Thus we assume region 3 is due to the shape of the rods. Error bars are two times standard error.

take place at completely unfeasible values of ϕ but are helpful as a base line. While we do not see precisely a straight line, as the slope appears to increase as ϕ increases, we see the diffusive region, and a region of roughly linear growth, with the slope increasing as the depletant fraction increases. This is due to the interaction between the AO and LJ potentials. The energy barrier is not precisely linear with ϕ, especially as ϕ reaches unfeasible values. We do not see regions 3 or 4; these regions only appear for simulations of two rod bundles breaking apart. Thus, we assert that the more complicated behaviour of Figure 3.6 is due to the shape of the rods. The rods can break apart in a piece wise fashion that is unavailable to individual particles. In particular, we expect the rods to be able to slide apart, and twist apart. We discuss these additional methods of escape later in this work.

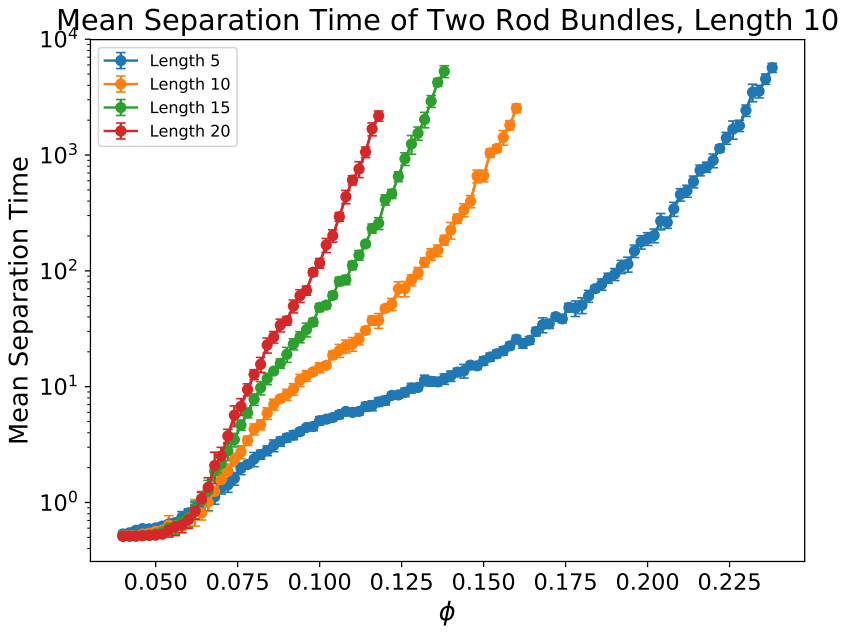

FIGURE 3.9: Plot of the mean separation time for a two rod bundle to break apart for rods with a persistence length of 1000, as a function of ϕ. All of the lengths we simulated had the 4 regions we saw in Figure 3.6. Error bars are two times standard error.

Figure 3.9 shows the results of simulations of over multiple rod lengths. We can see these same 4 regions appearing across multiple rod lengths. The range of ϕ over which region 3 occurs is dependent on the length of the rod. Region 3 is noticeable for the length 5 rods, but can barely be seen for the length 20 rods. Part of this can be explained by the fact that the longer rods have more excluded volume, and thus are more susceptible to changes in ϕ. Because of this, we end up speeding past region 3 for the longer rods because of this. Another feature is that, particularly for the short rods the slope of region 4 appears to be greater than the slope of region 2. This is similar behaviour to what we saw for 2 beads, where the slope was a bit steeper at the higher ϕ values.

These simulations were also run at different persistence lengths. Figure 3.10 shows the result of our simulations for rods with a persistence length of 100 σ_{sim}. These rods have a significantly lower persistence length than the rods we studied

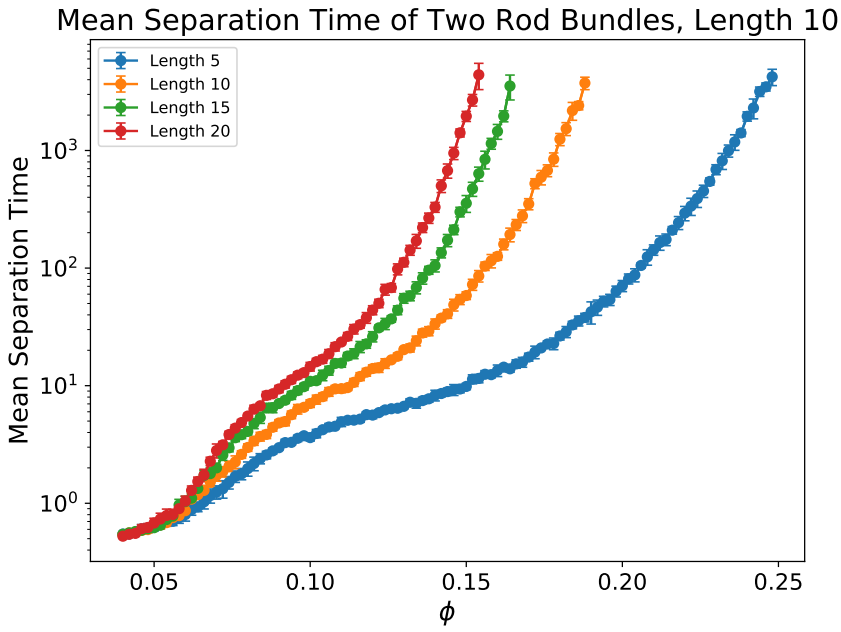

FIGURE 3.10: Plot of the average time for a two rod bundle to break apart for rods with a persistence length of 100, as a function of ϕ. The region of decreased mean separation time, starting at about $\phi = 0.08$, is significantly extended compared to Figure 3.9. Error bars are two times standard error.

thus far. We see the same four regions we found for the stiffer rods, but that region 3 is significantly extended for the flexible rods. This leads to shorter mean separation times after region 3 across all the rod lengths. These effects are more pronounced at longer rod lengths; comparing the length 20 rods between Figure 3.9 and Figure 3.10, region 3 is very short in 3.9, but clear in 3.10.

A rod of length 20 and persistence length 100 σ_{sim} has a Kuhn length of 200 σ_{sim}, which is significantly greater than its length. The colloids are within the rod-like limit even at the lowest persistence lengths and greatest rod lengths studied. However, decreasing the persistence length still significantly effects how the two rod bundle breaks apart. We believe that despite being within the rod-like limit, bundles of more flexible rods are able to break apart in a piece wise manner.

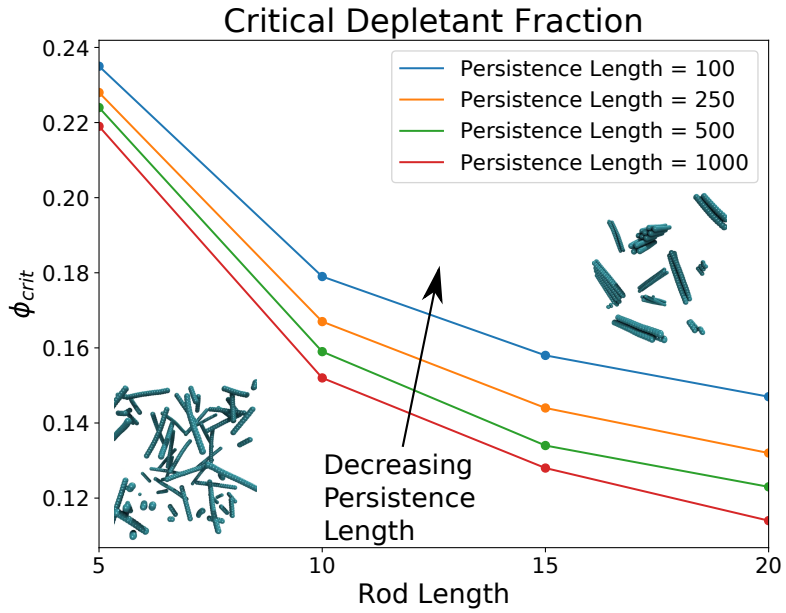

FIGURE 3.11: A plot of the critical depletant fraction for our two rod bundle simulations, in terms of rod length and persistence length. This can function as a phase plot. In our simulations, if a mixture of rods is above the line for their persistence length at a given length and ϕ, we predict that the they will form bundles

As stated before, in order for large bundles to form, two rod bundles must be sufficiently stable. If we take an average time to break apart of $1 \cdot 10^3 \tau$ as sufficiently stable, we can construct a plot of the critical depletant fraction ϕ_{Crit}, which is shown in Figure 3.11. For rods of lengths 10 to 20 and persistence length 1000 σ_{sim}, this gives us critical depletant fractions close to what we found in Figures 3.1 and 3.2. For rods of length 5 however, it significantly over estimates the required depletant fraction.

As stated before, analysis of two rod bundles neglects the rate at which additional rods will approach the two rod bundle and strengthen it. For the larger rods, this is a reasonable assumption. However, due to length 5 rods being the smallest rods we simulate, they diffuse the fastest because they have the least drag acting on them. This increased diffusion means that isolated rods can come into contact with small bundles more frequently, and that two rod bundles must

stay bundled for less time to form larger bundles. We believe this causes our two rod bundle simulations to significantly overestimate ϕ_{Crit} for our length 5 rods.

We see the critical depletant fraction decreases as the length of the rod increases, and we also see that decreasing the persistence length increases the critical depletant fraction. This is consistent with what we saw in Figure 3.10. Increasing the flexibility decreases the mean separation time, thus a larger value of ϕ is required to keep them bundled for $1 \cdot 10^3 \tau$.

Figure 3.11 can be used as a phase plot. For a given rod length and persistence length, ϕ values above the curve will form bundles while ϕ values below the curve will not.

3.3.1 Energy Between Rods At The Critical Depletant Fraction

Figure 3.12 shows the average energy between two rods in contact at the critical depletant fraction. Figure 3.12 shows that a decrease in stiffness increases the amount of energy required to keep the rods together. This is consistent with our other findings, as the more flexible rods required higher depletant fractions to stay bundled. Figure 3.12 also clearly shows that the critical energy increases as the length of the rod increases. Since increasing the rod length also increases the excluded volume associated with the rods being in the bundled state, and thus while the energy associated with two rod bundle at ϕ_{crit} goes up, ϕ_{crit} decreases as the rod length increases, as seen in Figure 3.11.

An entropic argument is the most straightforward explanation for the increase in energy required as you increase the length or decrease the stiffness. As the stiffness of the rods decreases, the rods have more configurations available in the unbundled state, where as in the bundled state, they are heavily restricted. Thus, there is a free energy gain associated with the unbundled state, and the energy between the two rods must be higher to keep the system in the bundled state. Similarly, as you increase the length of the rod, the entropy associated with the ability to freely rotate increases. Once again, there is a free energy gain associated with the unbundled state. With this argument, we expect the energy

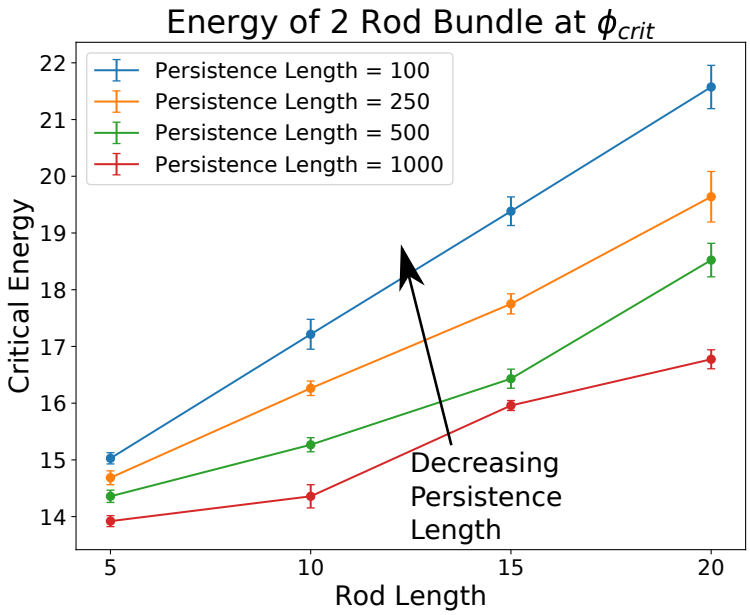

FIGURE 3.12: Plot of the energy between two rods, at the critical depletant fraction. We expect the energy required to keep bundles together to increase as we decrease the persistence length. In addition, the critical energy increases as the length of the rod increases. Error bars are two times standard error.

required to keep two rods together to be greater than that of a particle. We can extract ϕ_{Crit} from Figure 3.8 using the same definition as for two rod bundles, and find the energy associated with it from our simulations. When we do, we find that the critical energy is about 8 kT for 2 particles, significantly less than that of our two rod bundles.

3.3.2 2 Rod Bundles Breaking Apart

To supplement the entropic picture, we wanted to understand the specific physical mechanisms associated with the increased energy required to keep rods together for a certain amount of time compared to particles. The rods' different shape gives them access to multi-stage escape processes, where part of a rod can break free and reduce the effective energy barrier. We identify two additional

escape mechanisms available to the rods. The first is the ability of the rods to slide apart (Figure 3.13). Rods can slide laterally along one another, and reducing the excluded volume between the two rods, and thus reducing the effective energy barrier between the bundled and unbundled states. Note that they can also slide back into total side to side alignment.

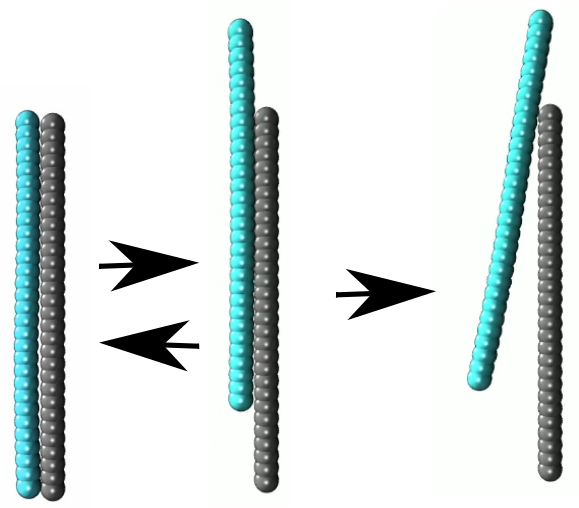

FIGURE 3.13: Pictures from simulations, demonstrating a rod sliding away from another. On the left, the rods are total side-to-side alignment. In the middle, they are partially displaced, reducing the effective energy barrier between the bundled and unbundled state. On the right, the rod breaks away due to the reduced energy barrier.

One note about sliding is that we do not see rods slide apart completely. Instead, we see a two step escape process, where the rods slide apart some amount, reduce the effective energy barrier, and then the rods break apart by other means. The main reason for this is that in our simulations, sliding is a slow process. Even though we have taken care to reduce the friction between of our rods, there are still potential energy wells due to their corrugated surface. These potential energy wells cause friction. By making smooth rods by using overlapping beads, we sought to minimize the size of these potential energy wells. However, in order for a rod to slide from being in total side-to-side alignment, to be being one bead offset, the rod must escape from as many of these potential

energy wells as there are beads on the rod. Thus, even our relatively smooth rods can still significantly inhibit sliding.

The second additional escape mechanism is the ability of the rods to twist apart, shown in Figure 3.14. With twisting, a large thermal kick can displace part of a rod, and move rods away from being parallel. This moves some of the beads on the rod out of range of the depletion force. As a result the energy binding the two rods goes down significantly. At this point, the bundle is not as likely to return to parallel as the energy barrier would suggest, as part of the rod is totally out of range of the depletion force. However, thermal fluctuations are acting on the entirety of the rod. Often two rods knocked away from parallel will diffuse away from one another rather than return to parallel.

FIGURE 3.14: Pictures from simulation, demonstrating a rod twisting apart from another. On the left, the rods are close to parallel. In the middle, a kick displaces the blue rod. From here, it can either return to parallel, or diffuse away. Since some of the rod is out of range of the depletion force, it is not as likely to return to parallel as the energy difference between the two states would suggest. On the right, the blue rod diffuses away from the black rod.

We expect both length and persistence length to effect the twisting process. In the case of length, the energy associated with keeping the rods bundled is distributed over the length of the rod. For longer rods, there is less energy at any piece of the rods than for short rods, and we expect this makes it easier to displace pieces of a long rod. As for the effect of persistence length, decreasing the persistence length decreases the correlation between adjacent beads on the rods. Thus it is easier for thermal fluctuations to kick small pieces of one rod

away from another. Thus, we expect the effect of rotation to increase as the length of the rods increases, and to increase as the persistence length decreases.

3.4 Restriction of Degrees of Freedom

In order to better understand the effect of these additional escape mechanisms available to the rods, we ran simulations where we used walls to restrict the movement of two rod bundles and suppress these mechanisms. In these simulations of two rod bundles, we set one of our two rods to be immovable, and the other to be free to move normally, and placed walls around our two rod bundle to restrict the ways the bundle could break apart. We implemented 3 possible restrictions. In the first, we restrict the rods' ability to slide by placing walls at either end of the long axis of the two rod bundle. This is why one of the rods needs to be immovable; if the bundle is free to rotate around, it can rotate away from the walls, at which point the sliding is no longer suppressed. This is the sliding restriction. In the second restriction, we suppress the rods' ability to

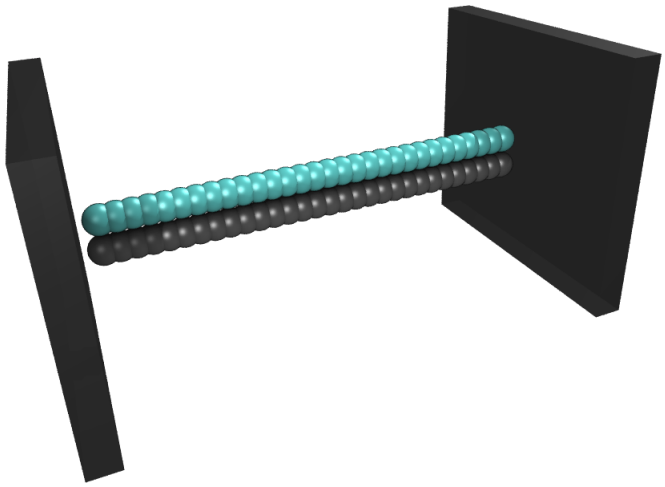

FIGURE 3.15: Picture of our sliding restriction. We place a wall at either end of the rod, lengthwise, to prevent it from sliding. The black rod is fixed in place to prevent the bundle from reorienting itself such that sliding is possible.

rotate by placing walls along either side of the 2 rod bundle, such that the free rod cannot rotate around the immovable rod. This is the rotation restriction. Finally in our third restriction we apply both these wall configurations together to restrict both of the escape mechanisms. This is the sliding and rotation restriction

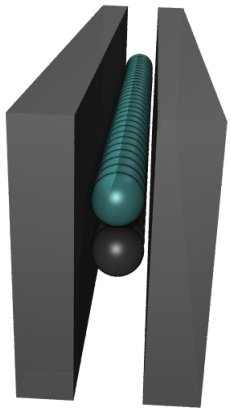

FIGURE 3.16: Picture of our rotation restriction. We place walls along the long side of both rods, to prevent the free blue rod from rotating around the black fixed rod.

In our analysis of two rod bundles, we found different behaviours in the growth of the mean separation time for rods (Figure 3.9) and particles (Figure 3.8), which we attributed to the rods' shape, and the escape mechanisms available to rods. Thus by suppressing these escape mechanisms we can isolate the effect of each. We ran Two Rod Bundle simulations with one of the rods fixed. In addition, we ran these simulations without any restriction, and with the sliding restriction, the rotation restriction, and the sliding and rotation restriction.

Figure 3.17 shows the results of these simulations for rods of length 10 and persistence length 1000 σ_{sim}. We will go through each of the restriction cases, starting with the unrestricted case. The unrestricted case is the case which is most similar to Figure 3.6. We see all four regions in the unrestricted case.

We also see all four regions when we view the sliding restricted case. Until about $\phi = 0.12$, the sliding restricted case is within error of the unrestricted case. After $\phi = 0.12$, the separation time of the sliding restricted case becomes

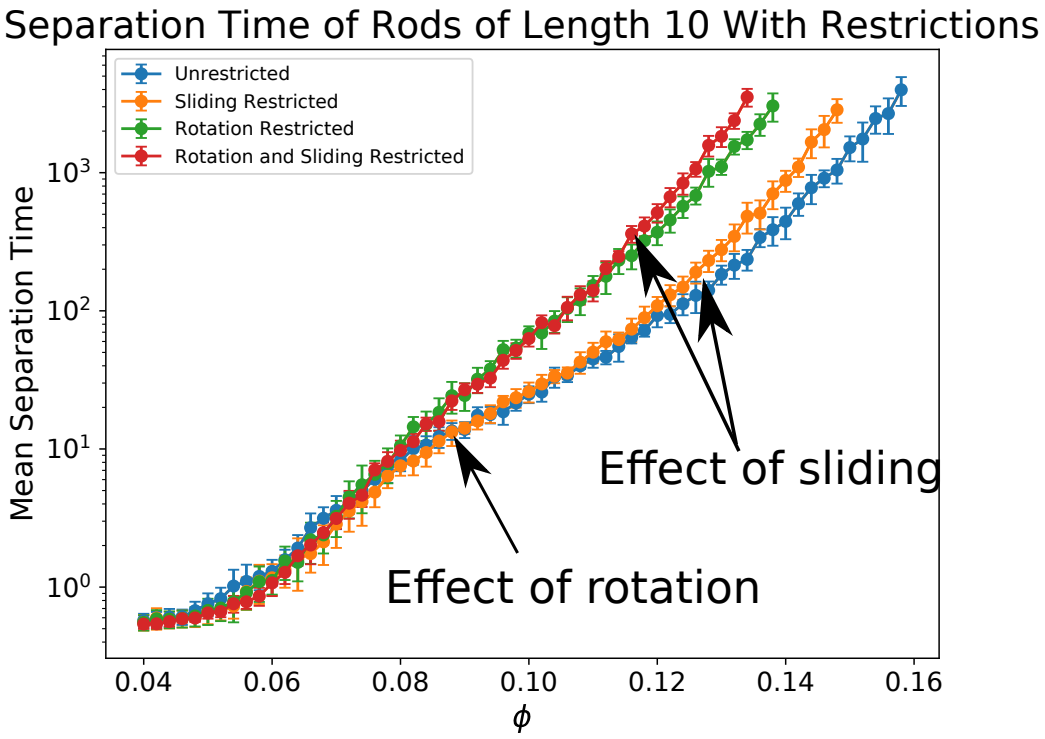

FIGURE 3.17: Plot of Time for Two Rod Bundle to Break Apart With Restricted Degrees of Freedom as a function of ϕ, for rods of length 10 and persistence length 1000 σ_{sim}. We identify a region around $\phi = 0.09$ where rotation effects become significant, and a region at $\phi = 0.13$ where sliding effects become significant. Error bars are two times standard error.

noticeably larger than the unrestricted case. We attribute this difference to the effect of sliding coming into play as the rods become bundled for long periods of time.

When we look at the rotation restricted case, we see the separation time is overlapped with the previous 2 cases until about $\phi = 0.09$, where we see the beginning of region 3 for the unrestricted and sliding restricted cases. However, for the rotation restricted case, we barely see a change in the behaviour of the separation time. The most striking difference between the separation time of particles and the separation time of rods was this region, and suppressing

rotation almost entirely eliminates it. Thus, we attribute the existence of region 3 almost entirely to rotation. In addition, this is the most dramatic change in the separation time as we restrict cases, so we believe the rods ability to rotate around one another is the main reason it takes more energy to keep two rods together than two particles. There is still a slight change in the slope at $\phi = 0.09$, which we attribute to the rods ability to break apart piecewise without rotating, but its effect is small compared to the effect of rotation.

Moving to the rotation and sliding restricted case, we see the sliding and rotation restriction line is on top of the rotation restricted line until about $\phi = 0.13$, where we see the separation time of the rotation restricted case become lower than that of the rotation and sliding restricted case. As before when we saw a similar difference in separation time between the sliding restricted and unrestricted cases, we attribute this difference to the effect of sliding. Qualitatively, sliding is a slow process; thus, the effect is only significant when the mean separation time is on the order of time it takes for rods to slide apart significantly.

In conclusion, we found that region 3 in Figure 3.6, which occurred only for rods, was primarily suppressed by restricting the rods ability to rotate. This was the most significant restriction. We also found restricting sliding to increase the mean separation time only when the mean separation time was relatively high. We believe that this is due to sliding being a slow process. Thus, it would not appear when the rods could not stay bundled long enough for it to matter.

3.5 Preferential Bundling

Earlier, we talked about using Figure 3.11 as a phase plot. If we consider a mixture of rods of different lengths, we can contrive a value of ϕ such that only rods above a certain length will form bundles. We ran a small number of simulations to show this effect qualitatively. We ran bundling simulations, with an equilibration phase of length $5 \cdot 10^2\tau$, a main simulation phase of $3 \cdot 10^3\tau$, and we omitted the data collection phase. Figure 3.18 shows the results of a simulation of 20 rods of length 5 and 20 rods of length 10, with $\phi = 0.18$. We see

the formation of large bundles of the longer rods, and that the shorter rods remain primarily free. However, this process is not perfect. Our definition of the critical depletant fraction was based on the stability of the two rod bundle, reasoning that it was a gateway to larger bundle formation. However, while the short rods cannot form large bundles independently, they can stick onto already formed bundles of long rods for significant periods of time, and skip the two rod bundle entirely. However, the difference in ϕ_{crit} between short and long rods is quite large, and as a result we do not expect the small rods to stay bundled for the length of the simulation. Thus most of the small rods will remain free, but some will be bundled with the larger rods.

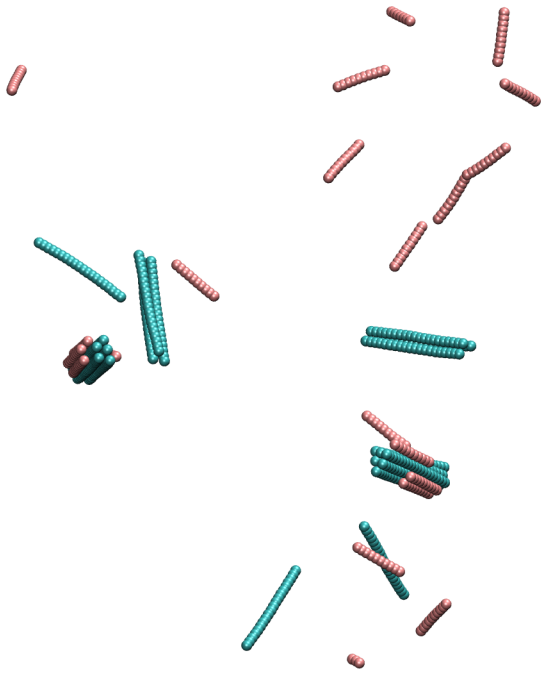

FIGURE 3.18: Picture from simulation of a mixture of short pink rods (length 5) and long blue rods (length 10). The long rods are mostly bundled, while the short rods are mostly free. While the short rods cannot form bundles on their own, they can stick onto bundles of long rods.

Since ϕ_{crit} increases as the persistence length of a rod goes down, we can do the same kind of preferential bundling with stiffness, where stiff rods will bundle

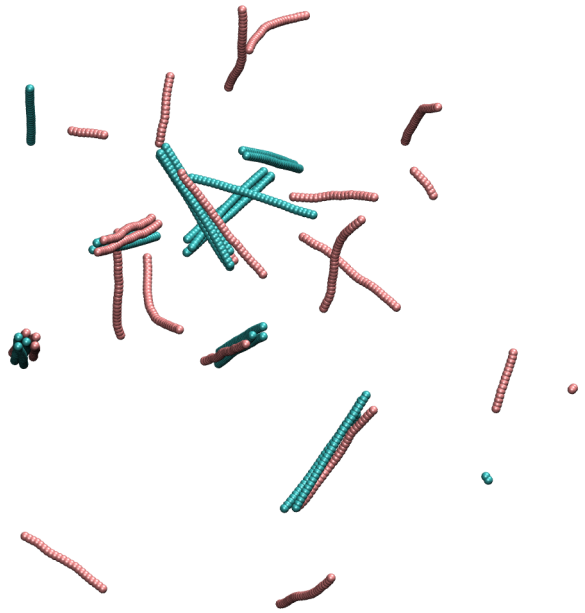

FIGURE 3.19: Picture from simulation of a mixture of flexible pink rods (Persistence length 100 σ_{sim}) and stiff blue rods (Persistence length 1000 σ_{sim}). The stiff rods are mostly bundled, while the flexible rods are mostly free. Here the flexible rods cannot form bundles on their own, but can stick to bundles of stiff rods.

and flexible rods will stay free. Figure 3.19 shows the result of a mixture of stiff (1000 σ_{sim}) and flexible rods (100 σ_{sim}) of length 30, with $\phi = 0.14$. The stiff rods form into bundles, while the flexible rods are primarily free. However, we see the same result as in the length case, where the flexible rods can skip the two rod bundle stage of bundle formation by sticking to a bundle of stiff rods. Here, most of the flexible rods are free, and most of the stiff rods are bundled, which we expect because the flexible rods cannot form small bundles on their own. However, because the difference in ϕ_{crit} is much less between stiff and flexible rods than the difference between long and short rods, if we ran this simulation for significantly longer, all the stiff rods would become bundled, and then all the flexible rods would be able to bundle with the bundles of stiff rods. However, we expect that during bundling process, significantly more stiff rods will be bundled than flexible rods.

Using Figure 3.11 as a phase plot is fine for a mixture of rods of the same length and persistence length, but care needs to be taken for mixtures of rods with different properties. Rods which cannot form large bundles on their own may still adhere to larger bundles. We expect this effect to become more significant if the difference between ϕ_{crit} between the two rod types is small. Since the difference in ϕ_{crit} between the shortest and longest rods we tested is much larger than the difference between the stiffest and most flexible rods, preferential bundling by stiffness seems to be less effective than preferential bundling by length. Nevertheless, preferential bundling by stiffness is still plausible if the difference in persistence length is large.

3.6 Hysteresis of Bundling

Our analysis in Section 3.2 suggested that large bundles are significantly more stable than small bundles of 2 or 3 rods. Because of this, it was plausible that large bundles were stable at values of ϕ where they were extremely unlikely to form. This could cause a hysteresis effect, where the behaviour of the system depends on its previous state. More specifically, if we start a simulation at a high value of ϕ, then slowly lower ϕ, the value of ϕ at which the bundles broke apart into isolated rods could be significantly lower than ϕ_{crit}.

To test this, we ran bundling simulations of 40 rods where we varied ϕ during the simulation. We ran an equilibration phase simulation for $5 \cdot 10^2 \tau$ to equilibrate the rods, then ran a main simulation for $3 \cdot 10^3 \tau$ under the effect of depletants, with ϕ starting at 0.1. Then we ran a data collection phase where we took data on the average number of isolated rods over $5 \cdot 10^2 \tau$. Then we increment ϕ by 0.01 and run another main simulation phase and data collection phase. We continue increasing ϕ and running simulation and data collection phases until $\phi = 0.17$. After running the simulations at $\phi = 0.17$, we begin decreasing ϕ by 0.01, and running the simulation and data collection phases, until we return to $\phi = 0.10$. For rods of length 10, we found previously that the critical depletant fraction was $\phi = 0.15$. Thus, this simulation will begin with the rods unbundled, and we will increase ϕ until $\phi = 0.17$. Since this is above ϕ_{crit}, we expect all the

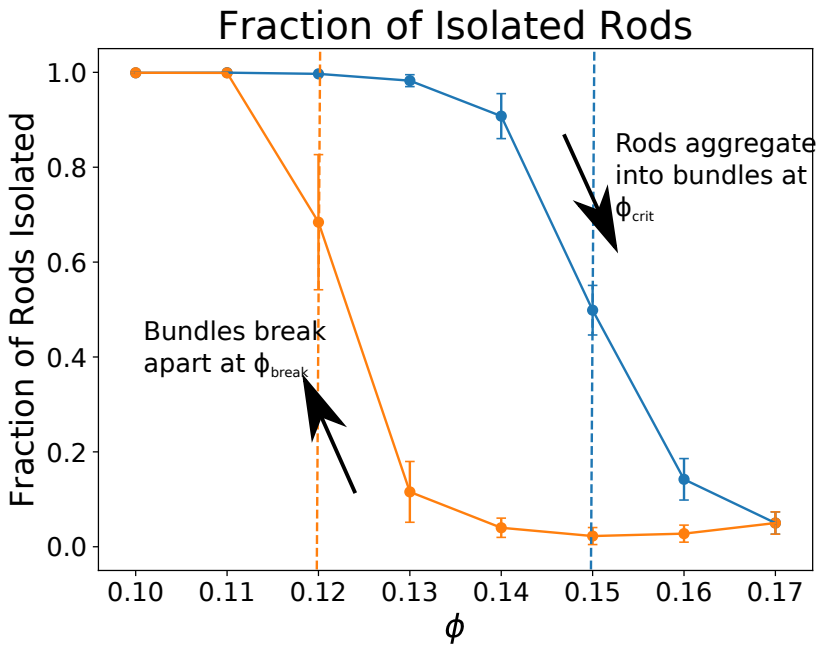

FIGURE 3.20: Plot of the fraction of rods isolated for our hysteresis simulations. The blue line represents the simulations where ϕ was increasing, and the yellow line represents simulations where ϕ was decreasing. Error bars are two times standard error.

rods to be bundled at this point. Once we begin decreasing ϕ, we expect to find a value of ϕ where the bundles break apart, ϕ_{break}. If the system exhibits hysteresis, we expect ϕ_{break} to be lower than ϕ_{crit}. We ran this simulation 10 times.

Figure 3.20 shows the results of these simulations. The blue line represents the results for simulations where ϕ is increasing, while the yellow line represents results for simulations where ϕ is decreasing. The increasing ϕ simulations show behaviour similar to Figure 3.1, where rods do not exhibit significant bundling below ϕ_{crit}, and are almost entirely bundled above ϕ_{crit}. At $\phi = 0.17$, almost all the rods are bundled, and remain bundled as ϕ decreases to 0.14. A small increase in the number of isolated rods is seen at $\phi = 0.14$ and 0.13, which we attribute to small (two to six rod) bundles in the simulation which break apart very quickly at the lower ϕ values. Finally, at $\phi = 0.12$, we see a significant increase in the number of isolated rods due to the break up of the large bundles.

Thus we say $\phi_{break} = 0.12$ for these simulations. The difference between ϕ_{crit} and ϕ_{break} is indicative of hysteresis.

ϕ_{break} is determined by the rate at which rods can escape from the large bundles. At $\phi = 0.14$ and 0.13, we see very little change in the large bundles within the simulation time, and thus at these depletant fractions, the rate at which rods separate from the large bundles is very low. While this is not compelling evidence that these structures are the equilibrium state of the system, it is very clear that these large bundles are very long lived compared to our simulation time at depletant fractions lower than ϕ_{crit}. Even at ϕ_{break}, we find that large bundles do not break apart completely within simulation time, although they do become significantly smaller. ϕ_{break} is the depletant fraction where the time taken for a rod to separate from a large bundle becomes significantly less than the simulation time. Thus we would expect the effect of this hysteresis to decrease if we increased the simulation time. However, given the separation time of a rod from a bundle at $\phi = 0.14$ and 0.13 appears to be very large, it is plausible that simulations ten times as long might not significantly change the behaviour of the system at these depletant fractions.

Chapter 4

Triple Helix Bundle Results

As discussed in the introduction, the UOttawa group conducted translocation experiments on both dsDNA and Triple Helix Bundles (3HB). When examining the number of folded translocations of these structures, they found that the 3HB folded significantly more than dsDNA. In fact, for 3HB translocations, the majority of events were folded. However, given that 3HB are roughly 3 strands of dsDNA stapled together, our expectation is that the 3HB should be significantly stiffer than dsDNA, and should fold less. We created two different models of the 3HB, and ran simulations of these models in a couple different situations.

4.1 Ribbon Model

4.1.1 Simulations of Polymer Translocation

The first simulations we ran were of our Ribbon model of 3HB, translocating through the pore. We wanted to see if the results would match with our expectations, that the 3HB should fold less than dsDNA without assistance, or if the results would match with UOttawa's results, where the 3HB folded more than dsDNA. Note that the ribbon model has a length of $100\sigma_{sim} = 200$ nm, while 3HB has an actual length of 820 nm. We simulate a shorter polymer because the full length would take much longer to simulate. We ran capture and translocation simulations with a pore of $r_{pore} = 3\sigma_{sim}$ and $t_{pore} = 3\sigma_{sim}$. This corresponded to a nanopore with a diameter of 12 nm and a thickness of 6 nm. The diameter corresponds to the pore size used by the UOttawa group, but our pore is half as

thick, due to a minor modelling error. We ran 1000 translocations of our ribbon model, and classified translocation events as either folded or unfolded. If the polymer translocated at a point within 10% of either end of the polymer, we consider the polymer to have threaded through the pore. If the polymer translocated at a point in the middle 80% of the polymer, the polymer is considered to have folded through the pore.

We also ran these simulations for a linear polymer with $l_p = 25\sigma_{sim}$, which corresponds to dsDNA persistence length. We consider this to be equivalent to dsDNA, and we will use this data as a benchmark. In addition, we wanted to account for the possibility of defects located on the 3HB. To this end, we proposed two modified ribbon models. The first is the Ribbon with Singular Defects, shown in Figure 4.1, where we induce defects at random points on the ribbon. Any given bead has a 20% chance of being defective, but the defects not necessarily lined up. This is to model a large number of weak defects.

FIGURE 4.1: Picture of a possible configuration of singular defects. The beads coloured blue are defects. We set 20 % of the beads on the 3HB to be defective.

Our second modified ribbon model is the Ribbon with Nunchuk Defect, shown in Figure 4.2. This model has three defects lined up at the center of the ribbon. This models a single strong defect, where the defect at the center effectively acts as a hinge for the halves of the ribbon. We thought this was evocative of a nunchuk.

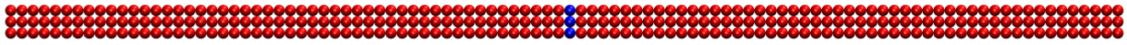

FIGURE 4.2: Picture of a nunchuk defect. The beads coloured blue are defects. These defects act as a hinge between the two halves of the 3HB; We thought this was evocative of a nunchuk.

A polymer in these simulations will either approach the pore by an end, or by the middle of the polymer. A polymer which approaches by an end will almost always thread through polymer by that end, and the entire polymer will be dragged through the pore. This is an unfolded translocation. If a polymer approaches by the middle, it will stuck with its middle above the pore. At this point, either some combination of thermal fluctuations and the electric field will fold the polymer through the pore, or the end of the polymer will find its way to the pore and thread through the pore. This process is shown in Figure 4.3. If the electric field is strong, a polymer with its middle at the pore will fold through very quickly. As the field decreases, it takes more time for polymer to fold through, and the probability that an end of the polymer finds its way to the pore increases.

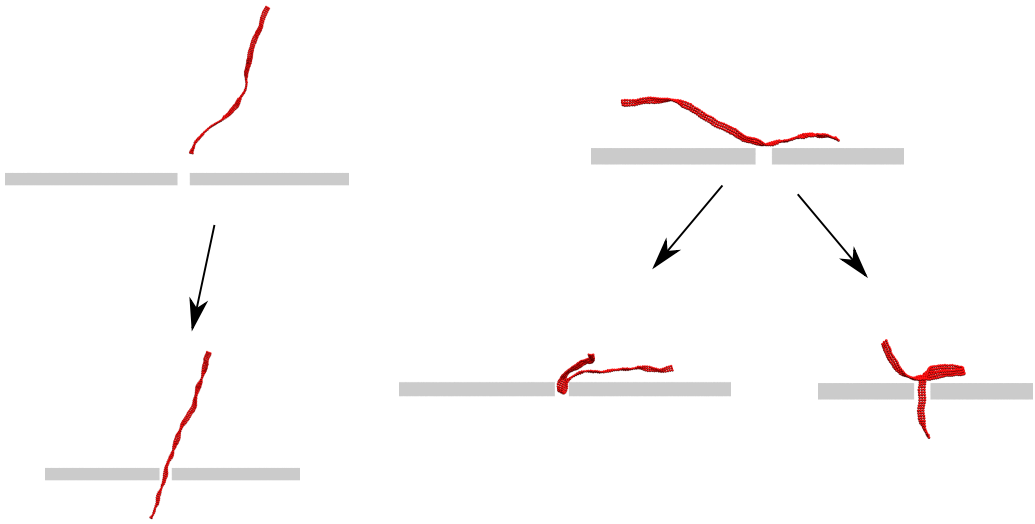

FIGURE 4.3: Pictures from simulations of the two approach possibilities. On the left, the polymer approaches by an end and threads through the pore. On the right, the polymer approaches by the middle of the polymer. Once there, it can either fold through, or stay stuck until an end finds the pore.

We expected 3HB to fold less than dsDNA were because the increased persistence length of 3HB should make it fold much slower. In addition, we expected the stiffer polymer to approach by an end more frequently, as it is elongated. We ran these simulations at voltages where the 3HB would fold

through the pore quite quickly, because we thought this scenario which would maximize the number of folded events for the 3HB. Adding defects should further increase the number of folded translocations by reducing the persistence length of the polymer, and making it easier to fold through the pore.

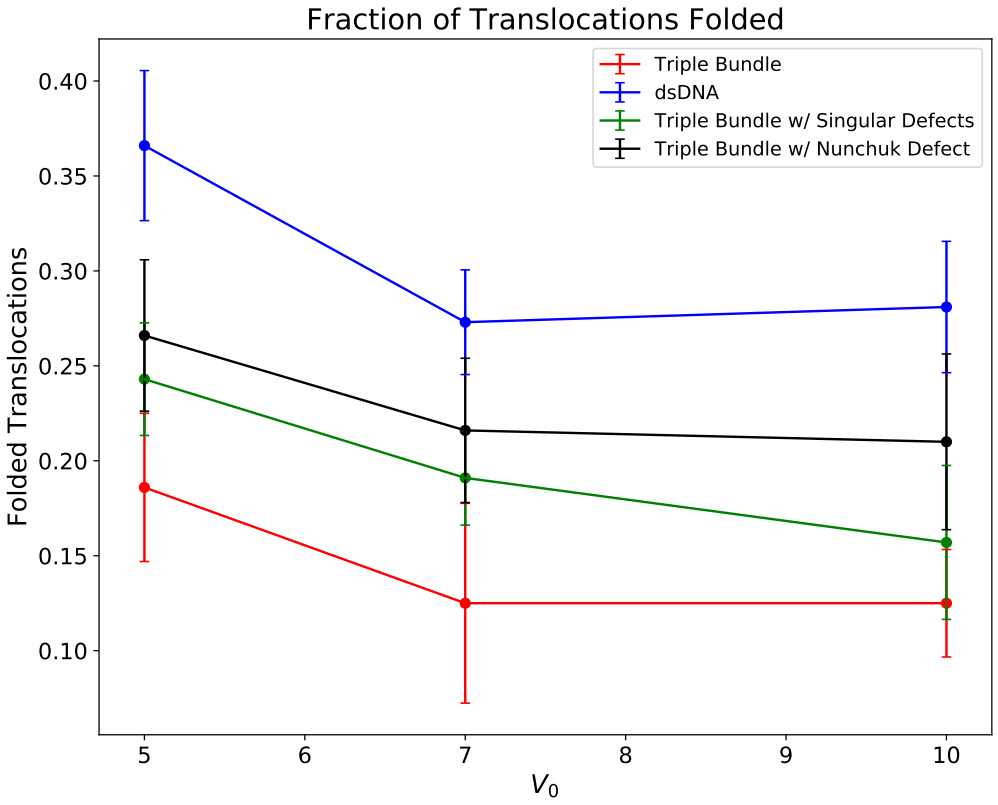

FIGURE 4.4: Plot of Fraction of Translocations Folded, as a function of voltage. We find dsDNA folds more than the 3HB at all voltages we tested, in contrast to experimental results. We added defects to possibly explain the difference, but the effects were not sufficient. Error bars are 2 times standard error

We ran these simulations over a couple different voltages. Figure 4.4 shows the results of these simulations. We see that dsDNA folds more than 3HB at all voltages we tested. This is consistent with our initial hypothesis that the 3HB

cannot fold more than dsDNA without some kind of help. Looking at our defective models, both fold more than 3HB, but neither model folded more than dsDNA. Inducing an effective joint at the middle with the nunchuk model increases the rate at which folded translocations occur much more than adding a large number of weak defects with the singular defects model. That being said, neither of them account for the amount of folding seen experimentally. It is important to note that our 3HB model is significantly shorter than the ones used in experiment, which could significantly affect the number of folded translocations.

Varying the voltage has an effect on how the polymer approaches the pore. Stronger electric fields will pull the polymer close to the pore in a more elongated configuration [8]. This will cause polymers to approach the pore by an end more frequently, and we expect polymer thread through the pore more frequently as well. Across all of our models, we see a drop in the number of folded translocations when we increase the voltage from 5 to 7, which is consistent with what we expect, but when we further increase the voltage to 10, we only see a significant drop for the ribbon with singular defects model. Varying the voltage also has an effect on how the polymer behaves at the pore, as stated before. However, the 3HB was only stuck at the pore for a significant period of time for $V_0 = 5$, and even then almost all of events which approached by the middle ended up folding through the pore, so we do not see an increase in the folded fraction when we increase the voltage.

Later on in the project we received compelling evidence that the 3HB could not fold through the pore easily. Thus these simulations are not directly comparable to the experiments performed by the UOttawa Group. Nonetheless, they can easily be relevant for experiments at higher voltages, and give insight more generally to how inducing defects can change folding behaviour at the pore.

4.1.2 Simulations of Lateral Diffusion

Experimental data from UOttawa showed 3HB being stuck at the pore for longer as voltage increases (Figure 1.8). This is not consistent with the idea that 3HB can fold through the pore on their own, without some sort of help. If 3HB can

fold through on their own, we would expect increasing the voltage increases the force 3HB feel at the pore, and 3HB should be pulled through the pore more easily. Thus, under these circumstances we expect the time stuck at the pore to go down as the voltage increases.

Consider this alternate picture for the folding of 3HB. If we assume that 3HB requires a defect to fold through the pore and cannot fold on their own at the pore, then the time that a polymer stays stuck at the pore is dependent on how long it takes for a defective part of 3HB to move over the pore and fold through. In this picture, the speed at which a polymer can move left-right along its length becomes meaningful. We call the polymer's ability to move left or right over the pore is its lateral diffusion. One way increasing the voltage of the system can decrease the lateral diffusion of the polymer is by increasing friction between the pore and the polymer.

We wanted to investigate lateral diffusion with our ribbon model. We modified the ribbon model such that $k_{angle} = 75\sigma_{sim}$ for each linear polymer on the ribbon. This effectively tripled the persistence length, so that the ribbon would never fold through the pore at the voltages we wanted to test. We used this stiff 3HB in lateral diffusion simulations. We ran these simulations with $r_{pore} = 3\sigma_{sim}$ and $t_{pore} = 3\sigma_{sim}$, and simulated at voltages between $V_0 = 3$ and $V_0 = 12$.

We considered the possibility that a weak defect, insufficient to allow 3HB to fold through, could inhibit diffusion independent of pore friction. We further modified our ribbon model such that the angle bonds acting on the 50th monomer of each linear polymer along the ribbon had $k_{angle} = 37.5\sigma_{sim}$, effectively inducing a half strength defect. This is similar to the nunchuk defect (Figure 4.2), except the defect is not completely flexible. We ran lateral diffusion simulations for these polymers, with the same pore as before, at voltages from $V_0 = 3$ to $V_0 = 10$.

Figure 4.5 shows the lateral diffusion of individual simulations as a function of time at $V_0 = 5$ and $V_0 = 10$. At the lower voltage, the closest monomer to the pore ranges from monomers 20 to 80 along the ribbon, but at the higher voltage this range is decreased to monomers 30 to 70 along the ribbon. Clearly the voltage is supressing the ribbons ability to laterally diffuse towards an end.

One note about these simulations is that over the full 30000 τ simulation time,

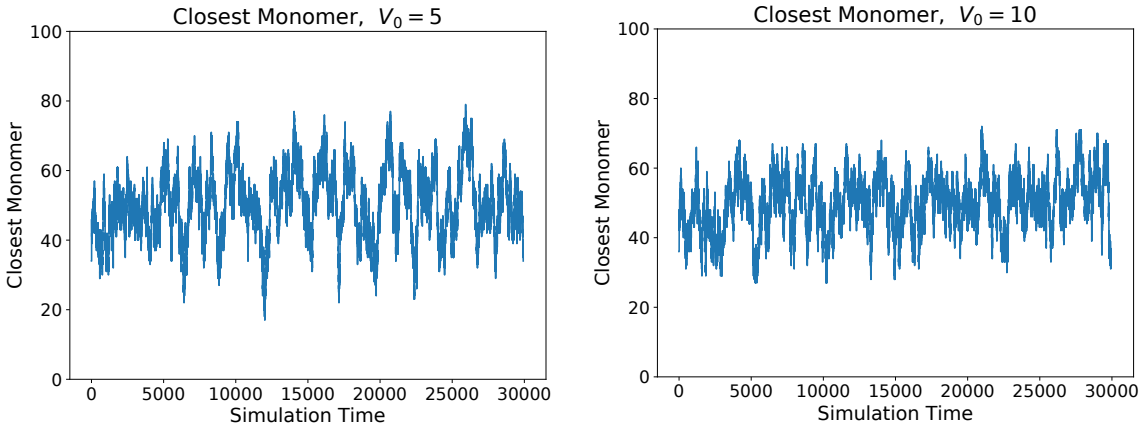

FIGURE 4.5: Closest Monomer to the pore over time, without a defect. Voltage significantly decreases the side to side motion.

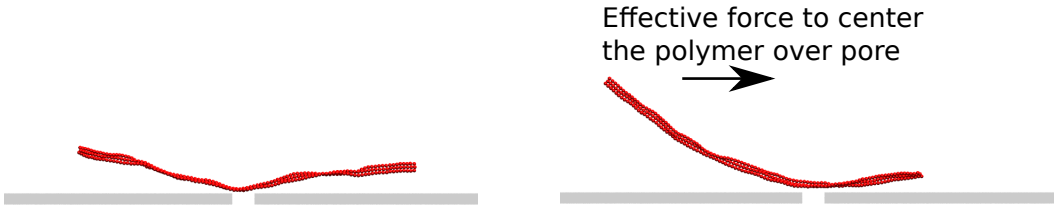

FIGURE 4.6: Pictures of the modified ribbon, from simulation. On the left the polymer is centered above the pore, which we see to be the favoured configuration. On the right, the polymer is off set, and the electric field exerts a force to center the polymer.

the polymers were never able to diffuse such that the end of a polymer was above the pore, and thread through the pore, even at the lowest voltages we tested. We expect pore friction to reduce the lateral diffusion, but it should not stop the polymer from diffusing such that an end is above the pore. We believe the suppression of side to side motion in these simulations is due to the fact that the electrical potential energy of a rod-like polymer is minimized when the polymer's center is above the pore. We expect the force pushing the polymer's center above the pore to be large when the center from the pore, and to go to zero as the polymer's center approaches the pore (Figure 4.6).

Figure 4.7 shows the results of the half strength defect simulations, at the

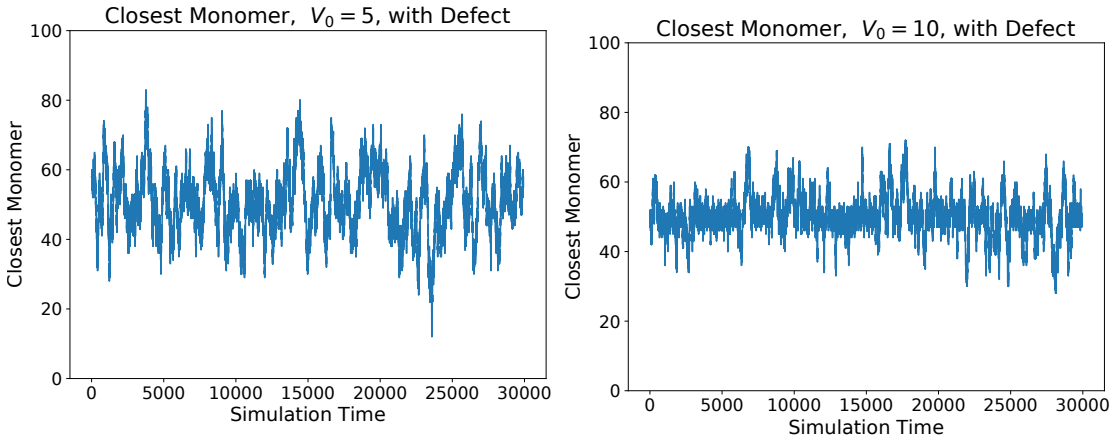

FIGURE 4.7: Closest Monomer to pore over time, with a half strength defect in the middle of the polymer. At $V_0 = 5$, the effect of the defect is not obvious, but at $V_0 = 10$, there are periods of time where the middle of the polymer is stuck at the pore for extended periods of time.

same voltages as Figure 4.5. At $V_0 = 5$, the trajectory looks similar to the simulations without a defect, but at $V_0 = 10$, we see that the polymer has large periods of time where the center of the polymer is stuck above the pore, as a result of the half strength defect being pulled into the pore. These stuck events clearly inhibit the polymer's lateral diffusion, and they become more prevalent as the simulation voltage increases. Figure 4.8 shows a picture from simulation of the half strength defect over the pore.

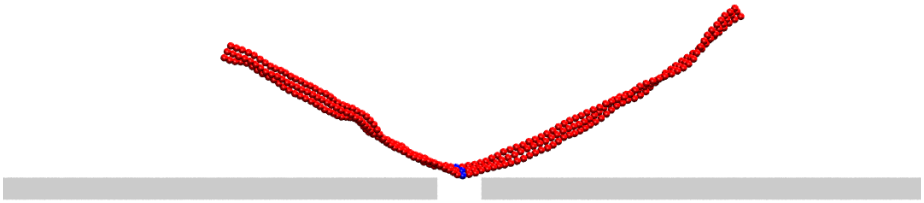

FIGURE 4.8: Picture from simulation of the half strength defect over the pore. The polymer is slightly pulled into the pore by the field due to the half strength defect.

We quantify the suppression of both the polymer being center above the pore, and the half strength defect inhibiting lateral movement by finding the standard

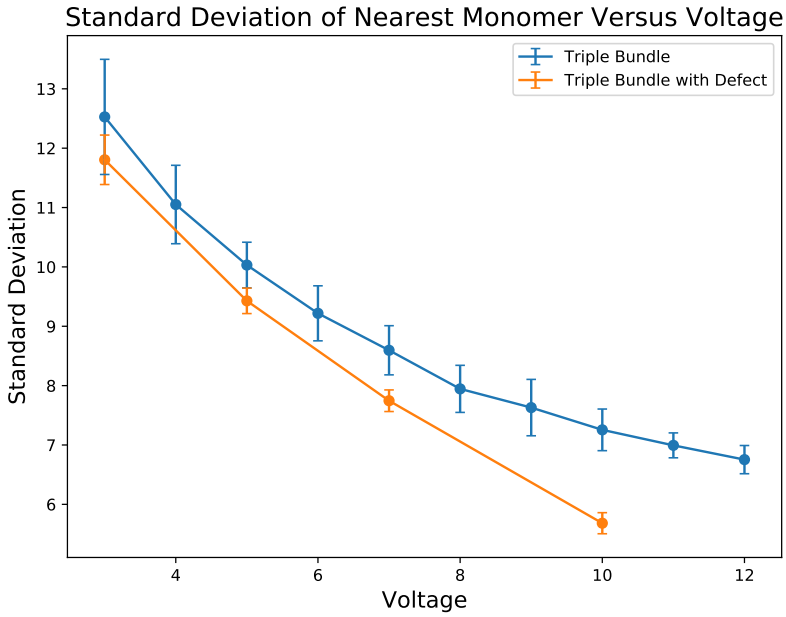

FIGURE 4.9: Standard deviation of the closest monomer as a function of applied voltage. Error bars are twice standard error. The first result is that, increasing voltage clear decreases the spread of positions the closest monomer can be at, thus decreasing the standard deviation. The second result is that adding a half strength defect at allows for the polymer's center to get at the pore, suppressing the lateral movement of the polymer.

deviation of the of the closest monomer, as the standard deviation will relate to the spread of the distribution of closest monomers. These results are shown in Figure 4.9. We see that increasing the voltage for a non-defective polymer clearly decreases the spread of the distribution of closest monomers, and that adding a defect further decrease the spread. The effect of the defect is more pronounced at higher voltages.

Relating these back to 3HB, the effect of centering the polymer above the pore is due to the rod-like structure of our modified ribbon. However, flexible polymers tend to get bunched up at the pore [23], and not lay flat across it. Thus, we do not expect this effect is significant for 3HB, although it does open up the possibility of confining rod-like objects at a nanopore. Stiff polymers getting

stuck at the pore, and unable to find an end has been seen in experiments [17], and our work can provide insight into that process. As for the effect of the half strength defect, since the modified ribbon will spend more time with its center above the pore than 3HB would, we expect Figure 4.9 to overstate its effect. While we see qualitative evidence of the polymer being stuck at the pore, it is difficult to disentangle its effect from the effect of the field. These simulations give insight into the effect of the defect, but a different simulation setup would be required to more extensively characterize it.

4.2 Linear Polymer With Defect Model

With compelling evidence that a defect was required to fold through, we wanted to run simulations of a polymer that could not fold through the pore without a defect. We were also concerned about the length of the polymer we were simulating. We wanted to model 3HB even more simply as a linear polymer. But even modelling 3HB as a linear polymer with a persistence length of 3 times dsDNA, $l_p = 150$ nm$= 75\sigma_{sim}$, the full 820 nm length of the would still be too large to simulate in an acceptable amount of time. Instead, we made a polymer which matched the ratio of length to Kuhn length of 3HB, and then chose the parameters of the pore such that it could not fold through on its own. Unfortunately, due to a modelling error we discovered late in the project, we matched this ratio to a polymer of length 1400 nm, about 5 Kuhn lengths. This error makes it difficult to compare the results directly to experimental results, but the simulations still give significant insight into the behaviour of polymers stuck at the pore. We modelled our polymer as a linear bead-chain polymer of 200 beads, and matching the ratio of length to persistence length gave us a polymer with $lp = 20\sigma_{sim}$. We then put a defect at the center of the polymer to allow it to fold through only at the center.

We took this polymer model and ran capture and translocation simulations with it. The pore in these simulations had $r_{pore} = 1.5\sigma_{sim}$ and $t_{pore} = 0$, and a voltage of $V_0 = 5$ was applied across the system. Due to our choice of polymer

and pore parameters, the polymer can only translocate through at the defect or at an end. We ran this simulation for 900 translocations.

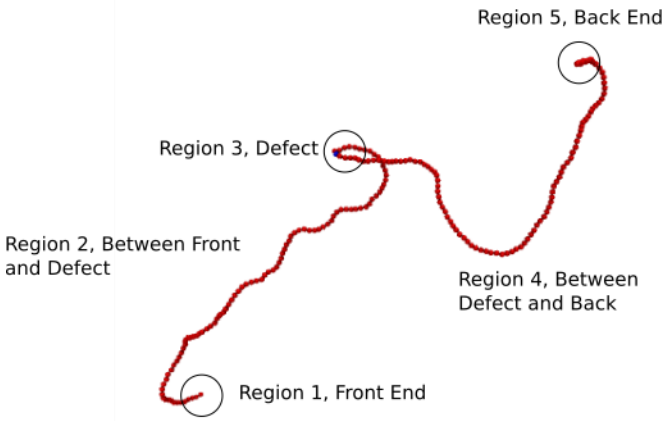

FIGURE 4.10: Description of regions

In these simulations we wanted to know how the polymer approached the pore, how the polymer translocated through the pore, and to see how different approaches could affect how the polymer translocated. To this end, whenever a monomer comes within $6\sigma_{sim}$ of the center of the pore, we record the closest monomer, and record this as the contact point. We classified approaching monomers by spliting the polymer up into 5 regions, as shown in Figure 4.10. Region 1 is the region within 10 beads of the front end. Region 3 is the region within 10 beads of the defect, while region 2 is just the space between regions 1 and 3. Region 5 is within 10 beads of the back of the polymer, and region 4 is the space between regions 3 and 5. The entire simulation procedure is detailed in Figure 4.11.

Figure 4.12 shows the results of these simulations. The first and most notable result is that the polymer is about equally likely to translocate by an end as by the defect. This result can give insight into the folding probability of a defective polymer, namely that the defect does significantly affect translocation dynamics. However, we expect this result to vary with polymer length and persistence length, so it can not be compared directly to the folding fraction of 3HB.

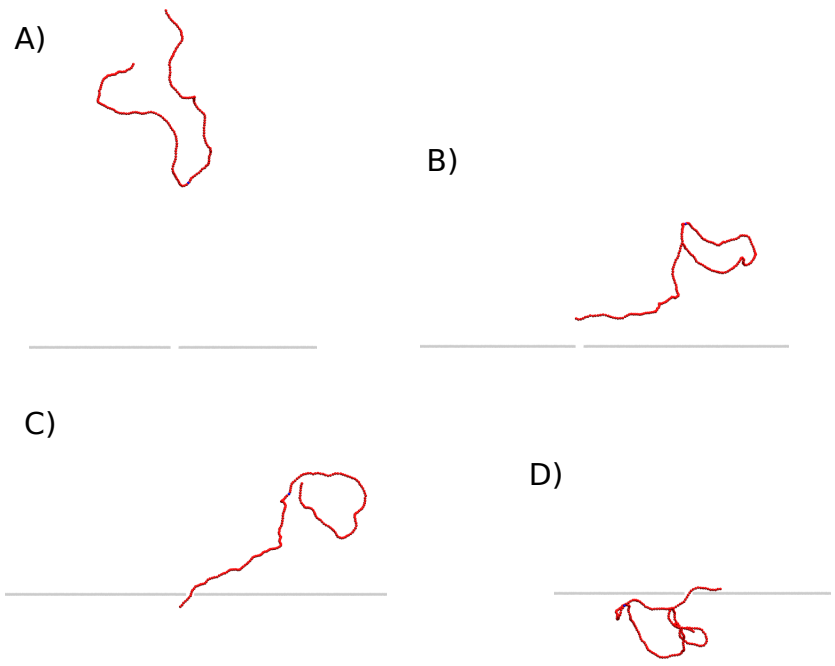

FIGURE 4.11: Simulation Process. A) Polymer is initialized far from the pore. B) Polymer approaches the pore. We record the closest monomer and classify how the polymer approached the pore; this polymer approaches from one of the ends. C) We record the monomer which threads through the pore; this polymer threads by the same end it approached by. D) Polymer finishes translocation.

Another result is that, while a full third of the events translocate by the defect, only about 5 percent actually approach the pore by the defect. It is not an unreasonable expectation that, since the defect is a joint, it might be equally likely to approach by the defect as by either end. However we do not see that in simulation. Instead, the polymer tends to unwrap as it approaches the pore [8]. As a result, there are significantly more translocation which approach by an end than by the defect.

Another result we see is that the location that a polymer approaches the pore at is highly correlated with how it translocates. Polymers which approach by end translocate by that end almost always. Polymers which approach by regions 2 or

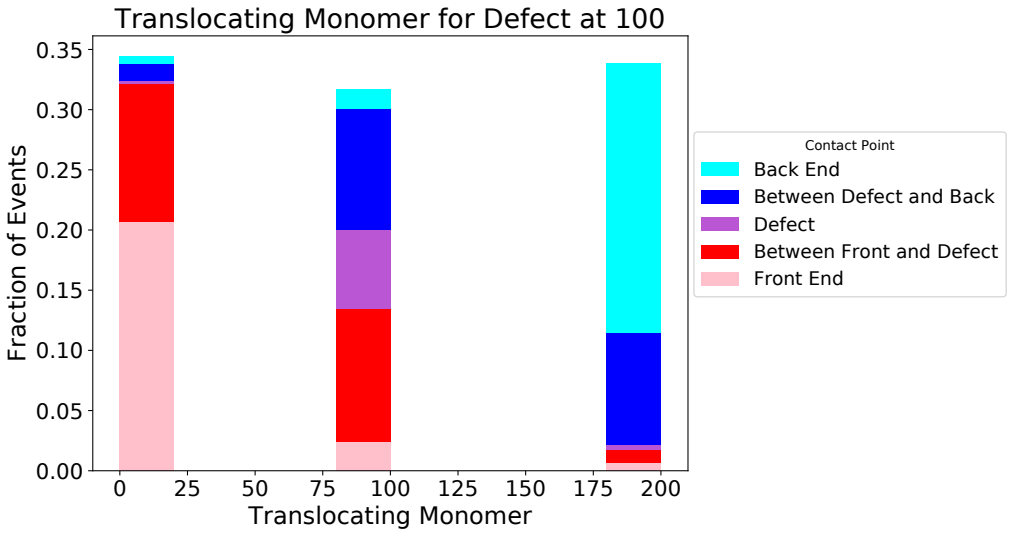

FIGURE 4.12: Plots for our simulations of polymers translocating with defects. The height of the bars indicates the number of polymers which translocated at that monomer. A polymer will translocate at either the front (The left most bar), the defect (The bar in the middle), or the back (The bar on the right). The colours on the bars represent the portion of events which approached by that region. The blue colours correspond to the back of the polymer, the red colours correspond to the front of the polymer, and the purple is the polymer approaching by a defect.

FIGURE 4.13: Pictures from simulation of a polymer getting stuck at the pore and getting bunched up. In this state, either end of the polymer could find the pore and thread through.

4 are about as likely to translocate by the closest end, or by the middle. Polymers which approach by the defect almost always translocate by the defect. This is what we would expect, the polymer is very likely to translocate close to where it approaches the pore. However, there is a small population of events which approach by one end, but translocate by the other end. One might think that in

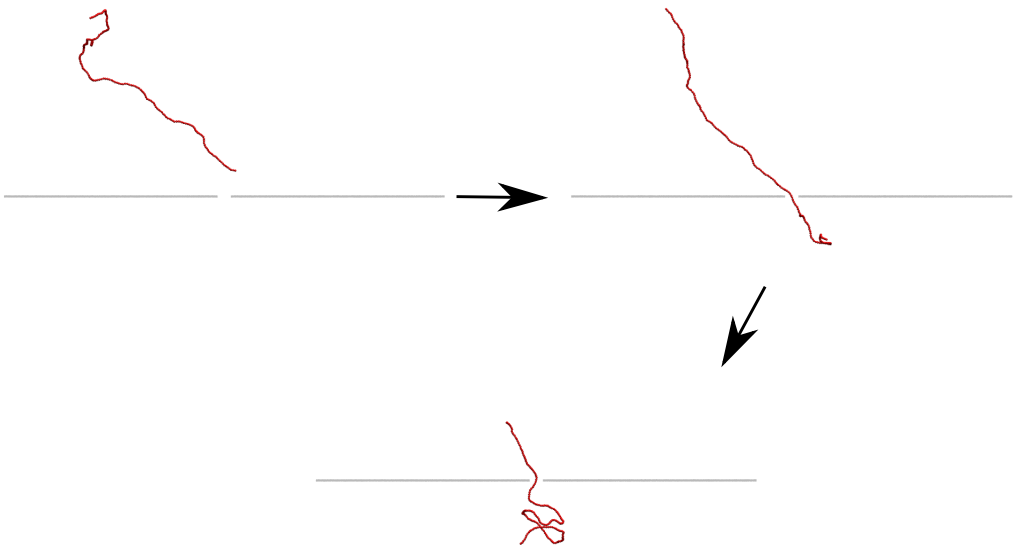

FIGURE 4.14: Pictures from simulation of a polymer approaching by an end and threading through very quickly.

these events, the polymer laterally diffuses along the polymer, over the defect, until the long end of the polymer is over the pore, but Figure 4.13 shows a what we see in simulation. Polymers which approach by region 2 or 4 tend to bunch up at the pore, since they cannot fold through. In this state, it is possible for either end of the polymer to get pulled to the pore and thread through. It is even plausible for the defect to find its way to the pore and fold through in the same way.

Polymers which approach from regions 1, 3, and 5 tend to thread through the pore and translocate very quickly. This is shown in Figure 4.14.

We quantify these different translocation behaviours by looking at the time between approach and translocation, as shown in Figure 4.15. Polymers which approach by an end or by the defect are over represented in the quick translocation events (less than 20 τ from approach to contact). The longer translocation events are dominated by the events which approach by a middle region. Both of these are consistent with what we see in simulation.

While the modelling error we found makes these results not directly applicable to 3HB, simulations of this kind still give us a wealth information about defective

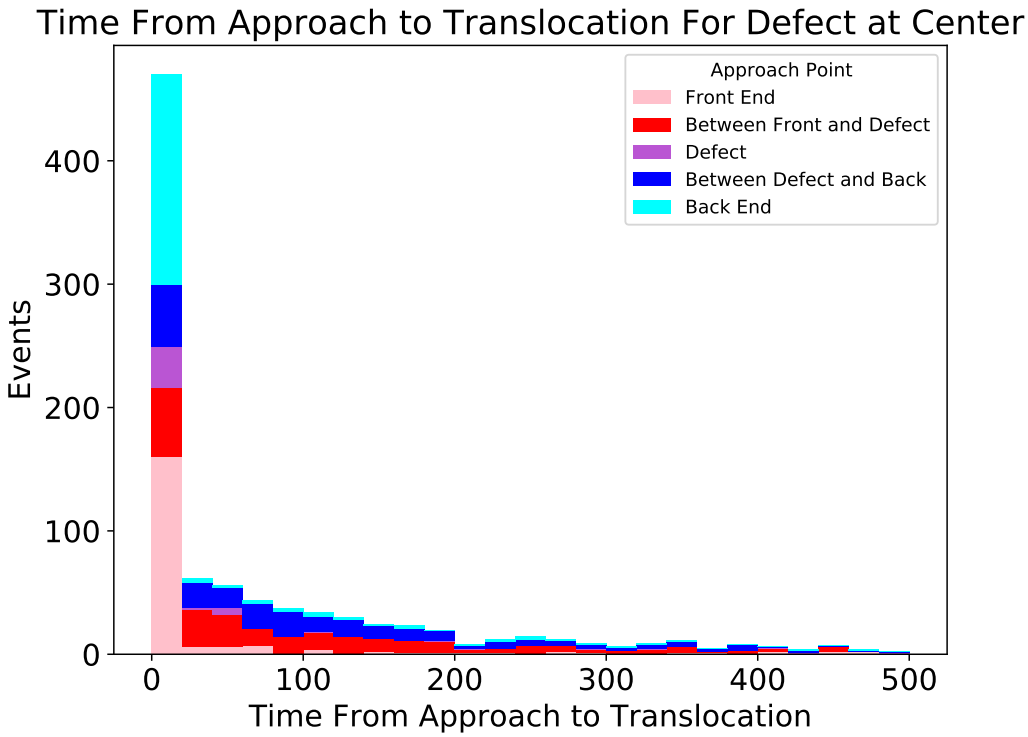

FIGURE 4.15: Histogram of time from approach to translocation. The fast translocation events (less than 20 τ) largely approach by an end or a defect, while the slow translocation events are dominated by events which approach by an intermediate region.

polymers, how they approach the pore, and how they translocate through the pore.

Chapter 5

Conclusion

5.1 Depletion Induced Bundling of Rod-Like Colloids

We used molecular dynamics to simulate systems of colloidal rods in a thermal bath, acting with an effective entropic force between them, depletion forces. We simulated both systems of many rods, and also performed detailed analysis of two rod bundles, and understanding the process by which two rod bundles break apart.

Our initial simulations of rods found a phase transition between the rods existing in an unbundled state, and bundled state, with the transition occurring at a critical depletant fraction. We found that this critical depletant fraction decreased as the length of the rod increased. We then proposed that at the densities we simulated, the two rod bundle was an extremely important step in bundle formation. We tried to relate the critical depletant in the simulations of many rods with the mean separation time of two rod bundles. We then found the energy between rods at the critical depletant fraction, and found that the energy associated with 2 rod bundles at the critical depletant fraction increased with rod length, and decreased with persistence length.

We found the mean separation time of two rod bundles breaking apart as a function of depletant fraction across many rod lengths and persistence lengths. We found that there was a regime of slower mean separation time growth, which was more prevalent for shorter rods. We then reasoned that this regime was due

to the shape of the rods, and proposed that the rods' shape allowed for additional escape mechanisms for a 2 rod bundle. These were sliding apart, and twisting apart.

We then ran simulations in which these additional escape mechanisms were suppressed. We first found that twisting apart was by far the dominant mechanism for rods breaking apart, with the rods' ability to slide only modestly decreasing the mean separation time. When we found the mean separation time of the rotation restricted two rod bundles, we found we could suppress the region of slower mean separation time growth.

We then ran simulations to demonstrate preferential bundling, where in a mixture of rods, only rods of certain characteristics would bundle. We demonstrated preferential bundling by length, where long rods would form bundles and short rods would remain unbundled. We also demonstrated preferential bundling by persistence length, where stiff rods would form bundles at a significantly higher rate than flexible rods. In the length case we found a population of short rods could be found bundled with long rods. In the persistence length case, we found that the flexible rods could be found bundled with stiff rods. This was significantly more prevalent in case of preferential bundling by stiffness. Future work for this topic would be focused on preferential bundling by stiffness, and maximizing the advantage that stiff rods have with respect to bundle formation.

Finally, we ran simulations showing the stability of large bundles of rods by demonstrating hysteresis in bundling. We found that large bundles of rods would dissociate into individual rods at a significantly lower depletant fraction than the critical depletant fraction.

Our initial simulations, and our emphasis on analyzing two rod bundles, mean our results are most pertinent for systems of rods at low densities. That being said, we believe that or analysis of two rod bundles may still be relevant at higher densities, particularly with respect to the effects of persistence length. In addition, while we used the depletion force as the main driver of bundling in these simulations, we believe that the results related to the energy required to bundle and the different mean separation time regimes would be relevant for any

attractive force between rod-like colloids.

We believe future work would largely be focused around the effects of persistence length on the bundling process. The simulation procedure for analyzing preferential bundling by length is currently insufficient, as we expect even the flexible rods to become bundled at very long time. A simulation procedure which takes in to account the large bundles precipitating out of solution is likely the best place to start. In addition, future work could also move out of the rod-like limit. Bundle formation is contingent on the rod shape of our colloids. If we continue to decrease the persistence length, we would expect a transition from bundle formation to less ordered structures.

5.2 Simulations of Triple Helix Bundles

We used molecular dynamics simulations to simulate the 3HB, dsDNA, and other model polymers to understand the structure of the Triple Helix Bundle and potential defects in the structure of the Triple 3HB, with the intention of providing insight into experiments performed by Vincent Tabard-Cossa's lab at UOttawa, which showed that the Triple Helix Bundle folded through nanopores more than dsDNA.

We started with simulations of dsDNA, our ribbon model of the 3HB, and defective models of the ribbon, ran at a couple different voltages, translocating through a nanopore. We found that dsDNA folded significantly more than the Triple Helix Bundle, and even when we added defects, while the defect models folded more than the Triple Helix Bundles, they were not sufficient to cause folding on the level of dsDNA.

Our next simulations we trying to analyze the lateral diffusion of a polymer. We simulated a modfied version of our ribbon model above the pore, and analyzed its' lateral diffusion. Our simulations suggested that a stiff polymer would be centered above the pore by the electric field of the nanopore. When we added a half strength defect to further impact lateral diffusion of the polymer, we found qualitative evidence that a defect, insufficient for the polymer to fold

through the pore, could inhibit lateral diffusion, but that the effect was complicated by the centering effect of the electric field.

We then ran simulations of defective linear polymers. We tried to match the ratio of length to persistence length with these polymers to the 3HB. We set simulation parameters such that the polymer could not fold through the nanopore without a defect. We found that, with the defect at the center of the polymer, the polymer would fold through the nanopore at the defect about as often as it would thread through the nanopore at one of the ends. We also found some more complicated dynamics. The polymer was significantly more likely to approach the pore by either end than it was by the defect. We found a population of events which approached the pore by the region between the defect and the front of the polymer, but eventually translocated by the back of the polymer; we reasoned that this was due to the polymer bunching up at the pore. This is further supported by our results showing that the majority of polymers which remain stuck at the pore for a significant period of time approach by the intermediate regions between the defect and either end. A significant modelling error made these simulations less applicable to 3HB than we would like, but they still give a rich picture of the dynamics of defect polymers approaching the nanopore and stuck at the nanopore.

Our work here was not able to explain the increased folding behaviour of 3HB found by the UOttawa group. He et al. (2023) [12] posited that the increased folding behaviour could be due to the stiff polymers approaching by an end, but due to slight misalignment with the pore do not immediately thread through, and are instead pinned at the pore. Investigation of this behaviour through simulations is an avenue for future work.

Bibliography

[1] Joshua A. Anderson, Jens Glaser, and Sharon C. Glotzer. "HOOMD-blue: A Python package for high-performance molecular dynamics and hard particle Monte Carlo simulations". In: *Computational Materials Science* 173 (2020), p. 109363. ISSN: 0927-0256. DOI: https://doi.org/10.1016/j.commatsci.2019.109363. URL: https://www.sciencedirect.com/science/article/pii/S0927025619306627.

[2] Sho Asakura and Fumio Oosawa. "Interaction between particles suspended in solutions of macromolecules". In: *Journal of Polymer Science* 33.126 (1958), pp. 183–192. DOI: https://doi.org/10.1002/pol.1958.1203312618. eprint: https://onlinelibrary.wiley.com/doi/pdf/10.1002/pol.1958.1203312618. URL: https://onlinelibrary.wiley.com/doi/abs/10.1002/pol.1958.1203312618.

[3] Eric Beamish, Vincent Tabard-Cossa, and Michel Godin. "Programmable DNA Nanoswitch Sensing with Solid-State Nanopores". In: *ACS Sensors* 4.9 (2019). PMID: 31449750, pp. 2458–2464. DOI: 10.1021/acssensors.9b01053. eprint: https://doi.org/10.1021/acssensors.9b01053. URL: https://doi.org/10.1021/acssensors.9b01053.

[4] Nicholas A W Bell and Ulrich F Keyser. "Digitally encoded DNA nanostructures for multiplexed, single-molecule protein sensing with nanopores". In: *Nature nanotechnology* 11.7 (2016), 645—651. ISSN: 1748-3387. DOI: 10.1038/nnano.2016.50. URL: https://doi.org/10.1038/nnano.2016.50.

[5] Michael Bruckman and Nicole Steinmetz. "Chemical Modification of the Inner and Outer Surfaces of Tobacco Mosaic Virus (TMV)". In: *Methods in molecular biology (Clifton, N.J.)* 1108 (Jan. 2014), pp. 173–85. DOI: 10.1007/978-1-62703-751-8_13.

[6] Seymour S. Cohen. "THE ISOLATION AND CRYSTALLIZATION OF PLANT VIRUSES AND OTHER PROTEIN MACRO MOLECULES BY MEANS OF HYDROPHILIC COLLOIDS". In: *Journal of Biological Chemistry* 144.2 (1942), pp. 353–362. ISSN: 0021-9258. DOI: https://doi.org/10.1016/S0021-9258(18)72516-7. URL: https://www.sciencedirect.com/science/article/pii/S0021925818725167.

[7] Alejandro Cuetos and Marjolein Dijkstra. "Kinetic Pathways for the Isotropic-Nematic Phase Transition in a System of Colloidal Hard Rods: A Simulation Study". In: *Phys. Rev. Lett.* 98 (9 2007), p. 095701. DOI: 10.1103/PhysRevLett.98.095701. URL: https://link.aps.org/doi/10.1103/PhysRevLett.98.095701.

[8] Farnoush Farahpour et al. "Chain deformation in translocation phenomena". In: *Soft Matter* 9 (9 2013), pp. 2750–2759. DOI: 10.1039/C2SM27416G. URL: http://dx.doi.org/10.1039/C2SM27416G.

[9] Hartmut Graf and Hartmut Löwen. "Phase diagram of tobacco mosaic virus solutions". In: *Phys. Rev. E* 59 (2 1999), pp. 1932–1942. DOI: 10.1103/PhysRevE.59.1932. URL: https://link.aps.org/doi/10.1103/PhysRevE.59.1932.

[10] Gary S. Grest and Kurt Kremer. "Molecular dynamics simulation for polymers in the presence of a heat bath". In: *Phys. Rev. A* 33 (5 1986), pp. 3628–3631. DOI: 10.1103/PhysRevA.33.3628. URL: https://link.aps.org/doi/10.1103/PhysRevA.33.3628.

[11] Liqun He. "DNA Nanostructures for Nanopore-Based Digital Assays". PhD thesis. University of Ottawa, 2022.

[12] Liqun He et al. "DNA origami characterized via solid-state nanopore: Insights into nanostructure dimensions, rigidity and yield". In: *ChemRxiv* (2023). DOI: 10.26434/chemrxiv-2023-s0vmn.

[13] J. E. Jones. "On the Determination of Molecular Fields. II. From the Equation of State of a Gas". In: *Proceedings of the Royal Society of London Series A* 106.738 (Oct. 1924), pp. 463–477. DOI: 10.1098/rspa.1924.0082.

[14] H.A. Kramers. "Brownian motion in a field of force and the diffusion model of chemical reactions". In: *Physica* 7.4 (1940), pp. 284–304. ISSN: 0031-8914. DOI: https://doi.org/10.1016/S0031-8914(40)90098-2. URL: https://www.sciencedirect.com/science/article/pii/S0031891440900982.

[15] Lev Davidovich Landau and Evgenii Mikhailovich Lifshitz. *Statistical Physics: Volume 5*. Vol. 5. Elsevier, 2013.

[16] T.L. Madden and J. Herzfeld. "Crowding-induced organization of cytoskeletal elements: I. Spontaneous demixing of cytosolic proteins and model filaments to form filament bundles". In: *Biophysical Journal* 65.3 (1993), pp. 1147–1154. ISSN: 0006-3495. DOI: https://doi.org/10.1016/S0006-3495(93)81144-5. URL: https://www.sciencedirect.com/science/article/pii/S0006349593811445.

[17] Angus McMullen et al. "Stiff filamentous virus translocations through solid-state nanopores". In: *Nature communications* 5 (2014), p. 4171. ISSN: 2041-1723. DOI: 10.1038/ncomms5171. URL: https://doi.org/10.1038/ncomms5171.

[18] Austin Nehring, Tyler N Shendruk, and Hendrick W de Haan. "Morphology of depletant-induced erythrocyte aggregates". eng. In: *Soft matter* 14.4 (2018), pp. 816–8171. ISSN: 1744-683X.

[19] Paul Rothemund. "Folding DNA to create nanoscale shapes and patterns". In: *Nature* 440 (Mar. 2006).

[20] Nima Saeidi et al. "Molecular crowding of collagen: A pathway to produce highly-organized collagenous structures". In: *Biomaterials* 33.30 (2012), pp. 7366–7374. ISSN: 0142-9612. DOI: https://doi.org/10.1016/j.biomaterials.2012.06.041. URL: https://www.sciencedirect.com/science/article/pii/S0142961212006916.

[21] Gert R Strobl and Gert R Strobl. *The physics of polymers*. Vol. 2. Springer, 1997.

[22] R. Tharmann, M.M.A.E. Claessens, and A.R. Bausch. "Micro- and Macrorheological Properties of Actin Networks Effectively Cross-Linked by Depletion Forces". In: *Biophysical Journal* 90.7 (2006), pp. 2622–2627. ISSN: 0006-3495. DOI: https://doi.org/10.1529/biophysj.105.070458. URL: https://www.sciencedirect.com/science/article/pii/S0006349506724432.

[23] Sarah C Vollmer and Hendrick W de Haan. "Translocation is a nonequilibrium process at all stages: Simulating the capture and translocation of a polymer by a nanopore". In: *The Journal of chemical physics* 145.15 (2016), p. 154902.

[24] John D. Weeks, David Chandler, and Hans C. Andersen. "Role of Repulsive Forces in Determining the Equilibrium Structure of Simple Liquids". In: *The Journal of Chemical Physics* 54.12 (1971), pp. 5237–5247. DOI: 10.1063/1.1674820. eprint: https://doi.org/10.1063/1.1674820. URL: https://doi.org/10.1063/1.1674820.

[25] Yasheng Yang and Michael F. Hagan. "Theoretical calculation of the phase behavior of colloidal membranes". In: *Physical Review E* 84.5 (2011). DOI: 10.1103/physreve.84.051402. URL: https://doi.org/10.1103%2Fphysreve.84.051402.

Appendix A

Correlations Along The Polymer

When speaking about worm like chains in section 2.2.4 of this thesis, we said that the average correlation between two tangent vectors on a worm-like chain was, from Landau and Lifshitz (2013)

$$\langle cos\theta_{i,j} \rangle = e^{-\frac{l_{i,j}}{l_p}} \tag{A.1}$$

Where $\theta_{i,j}$ is the angle between the lines tangent to the chain at points i and j, $l_{i,j}$ is the length along the chain between points i and j, and l_p is the persistence length.

However, it is not obvious that the correlations should decay as a simple exponential. This section contains a more detailed explanation of this form. The work in this appendix is essentially following the derivation of the persistence length of a worm-like chain from page 399 of Landau and Lifshitz (2013), in order to make it more clear why the correlations between vectors tangent to the polymer must decay exponentially.

Let us begin with a length of a worm-like chain. We pick three arbitrary points on it; a, b, and c. We will take the unit vector tangent to the chain at a to be $\vec{A}$, the unit vector tangent to the chain at b to be $\vec{B}$, and the unit vector tangent to the chain at c to be $\vec{C}$. Finally, we will take the length along the chain from a to b to be l_{ab}, the length along the chain from b to c to be l_{bc}, and the length along the chain from a to c to be l_{ac}.

From the Binet-Cauchy Identity, we can say

$$(\vec{A} \times \vec{B}) \cdot (\vec{B} \times \vec{C}) = (\vec{A} \cdot \vec{B})(\vec{B} \cdot \vec{C}) - (\vec{B} \cdot \vec{B})(\vec{A} \cdot \vec{C}) \tag{A.2}$$

$(\vec{B} \cdot \vec{B}) = 1$, thus we can say

$$(\vec{A} \cdot \vec{C}) = (\vec{A} \cdot \vec{B})(\vec{B} \cdot \vec{C}) - (\vec{A} \times \vec{B}) \cdot (\vec{B} \times \vec{C}) \tag{A.3}$$

Now we want to express this in terms of angle between the tangent vectors.

$$cos\theta_{AC} = cos\theta_{AB} cos\theta_{BC} - sin\theta_{AB} sin\theta_{BC} cos\phi \tag{A.4}$$

Where θ_{AC} is the angle between vectors $\vec{A}$ and $\vec{C}$, θ_{AB} is the angle between vectors $\vec{A}$ and $\vec{B}$, θ_{BC} is the angle between vectors $\vec{B}$ and $\vec{C}$, and ϕ is the angle between $(\vec{A} \times \vec{B})$ and $(\vec{B} \times \vec{C})$.

Now we will take the average of both sides

$$\langle cos\theta_{AC} \rangle = \langle cos\theta_{AB} cos\theta_{BC} \rangle - \langle sin\theta_{AB} sin\theta_{BC} cos\phi \rangle \tag{A.5}$$

Here, Landau and Lifshitz notes that the fluctuations in the curvature between a and b, and between b and c are statistically independent. Thus we can say $\langle sin\theta_{AB} sin\theta_{BC} cos\phi \rangle = 0$, and $\langle cos\theta_{AB} cos\theta_{BC} \rangle = \langle cos\theta_{AB} \rangle \langle cos\theta_{BC} \rangle$ leaving us with

$$\langle cos\theta_{AC} \rangle = \langle cos\theta_{AB} \rangle \langle cos\theta_{BC} \rangle \tag{A.6}$$

Now we want to note that we want correlations as a function of length

$$\langle cos\theta_{AC} \rangle = f(l_{ac}) \tag{A.7}$$

Now Equation A.6 says

$$f(l_{ac}) = f(l_{ab}) f(l_{bc}) \tag{A.8}$$

And noting that the locations of a, b, and c are arbitrary, and that $l_{ac} = l_{ab} + l_{bc}$, we can see

$$f(a+b) = f(a)f(b) \tag{A.9}$$

Which implies $f(l)$ is an exponential function. Noting that the $f(0) = 1$ and that the correlations should go to zero as l approaches infinity, we can see that a simple exponential decay in space can satisfy all of these conditions. At this point, Landau and Lifshitz matches the exponential decay to it's short time behaviour to find the characteristic length. We will take a simpler approach. Once we know that the $\langle cos\theta_{i,j} \rangle$ decays exponentially, we can define the persistence length as the characteristic length over which correlations decay, and thus

$$\langle cos\theta_{i,j} \rangle = e^{-\frac{l_{i,j}}{l_p}} \tag{A.10}$$